# Dysregulation of mannose-6-phosphate–dependent cholesterol homeostasis in acinar cells mediates pancreatitis

Olga A. Mareninova,[1,2] Eszter T. Vegh,[1,3] Natalia Shalbueva,[1,2] Carli J.M. Wightman,[1,2] Dustin L. Dillon,[1,2] Sudarshan Malla,[1] Yan Xie,[4] Toshimasa Takahashi,[5] Zoltan Rakonczay Jr.,[3] Samuel W. French,[6] Herbert Y. Gaisano,[5] Fred S. Gorelick,[7] Stephen J. Pandol,[8] Steven J. Bensinger,[9] Nicholas O. Davidson,[4] David W. Dawson,[10] Ilya Gukovsky,[1,2] and Anna S. Gukovskaya[1,2]

[1]Department of Medicine, David Geffen School of Medicine at UCLA, Los Angeles, California, USA. [2]VA Greater Los Angeles Healthcare System, Los Angeles, California, USA. [3]Department of Pathophysiology, University of Szeged, Szeged, Hungary. [4]Division of Gastroenterology, Washington University School of Medicine, St. Louis, Missouri, USA. [5]Department of Medicine, University of Toronto, Toronto, Ontario, Canada. [6]Department of Pathology, Harbor-UCLA Medical Center, Torrance, California, USA. [7]Departments of Cell Biology and Internal Medicine, Yale University School of Medicine and VA West Haven, West Haven, Connecticut, USA. [8]Department of Medicine, Cedars-Sinai Medical Center, Los Angeles, California, USA. [9]Departments of Microbiology, Immunology and Molecular Genetics and [10]Department of Pathology and Laboratory Medicine and Jonsson Comprehensive Cancer Center, David Geffen School of Medicine at UCLA, Los Angeles, California, USA.

**Disordered lysosomal/autophagy pathways initiate and drive pancreatitis, but the underlying mechanisms and links to disease pathology are poorly understood. Here, we show that the mannose-6-phosphate (M6P) pathway of hydrolase delivery to lysosomes critically regulates pancreatic acinar cell cholesterol metabolism. Ablation of the *Gnptab* gene encoding a key enzyme in the M6P pathway disrupted acinar cell cholesterol turnover, causing accumulation of nonesterified cholesterol in lysosomes/autolysosomes, its depletion in the plasma membrane, and upregulation of cholesterol synthesis and uptake. We found similar dysregulation of acinar cell cholesterol, and a decrease in GNPTAB levels, in both WT experimental pancreatitis and human disease. The mechanisms mediating pancreatic cholesterol dyshomeostasis in *Gnptab*$^{-/-}$ and experimental models involve a disordered endolysosomal system, resulting in impaired cholesterol transport through lysosomes and blockage of autophagic flux. By contrast, in *Gnptab*$^{-/-}$ liver the endolysosomal system and cholesterol homeostasis were largely unaffected. *Gnptab*$^{-/-}$ mice developed spontaneous pancreatitis. Normalization of cholesterol metabolism by pharmacologic means alleviated responses of experimental pancreatitis, particularly trypsinogen activation, the disease hallmark. The results reveal the essential role of the M6P pathway in maintaining exocrine pancreas homeostasis and function, and implicate cholesterol disordering in the pathogenesis of pancreatitis.**

## Introduction

Pancreatitis is a common, potentially fatal disease of the exocrine pancreas. Its pathogenesis remains obscure, and no specific or effective treatment is available (1, 2). Because of the general lack of access to human tissue, most studies use animal or ex vivo (cellular) models to investigate pathogenic mechanisms of pancreatitis (3). These models reproduce pathologic responses of human disease and the spectrum of their severity. Although defects in other cell types' function (e.g., ductal; ref. 4) can initiate pancreatitis, damaged acinar cells play a central role in the disease development (1, 5). The primary function of these cells is to synthesize, store, and export digestive enzymes, which relies on coordinated actions of cytoplasmic organelles to maintain membrane trafficking along secretory and endolysosomal pathways (5).

Recent studies indicate that lysosomal/autophagy pathways are impaired in acinar cells in both experimental and human pancreatitis (5–7). Further, genetic alterations specifically targeting autophagy or lysosomal function can cause spontaneous pancreatitis in mice (8–11). However, the mechanisms whereby impaired lysosomal/autophagy pathways cause disordering of key acinar cell organelles, e.g., the ER and mitochondria, and classic pancreatitis responses, such as inappropriate, intra-acinar trypsinogen activation, are poorly understood (5, 7).

Delivery of newly synthesized hydrolases to lysosomes involves covalent addition of mannose 6-phosphate (M6P) to asparagine residues of lysosomal hydrolases in the *cis*-Golgi network. The modified hydrolases then bind to one of the two transmembrane M6P receptors on vesicles that are subsequently directed toward endosomes to deliver their cargo to lysosomes (12–15). N-acetylglucosamine-1-phosphotransferase is a key enzyme in the M6P-tag formation; its catalytic α/β subunits are encoded by the *GNPTAB* gene (15–17). Ablation of *Gnptab* in mice (18, 19) causes pathologic changes in exocrine glands, including the pancreas, the main manifestation of which is accumulation of large vacuoles identified by electron microscopy as autolysosomes (19). Accumulation of large vacuoles in acinar cells is

**Authorship note:** OAM, ETV, and NS contributed equally. SWF is deceased.
**Conflict of interest:** The authors have declared that no conflict of interest exists.

**Submitted:** December 14, 2020; **Accepted:** June 11, 2021; **Published:** August 2, 2021.
**Reference information:** *J Clin Invest*. 2021;131(15):e146870.
https://doi.org/10.1172/JCI146870.

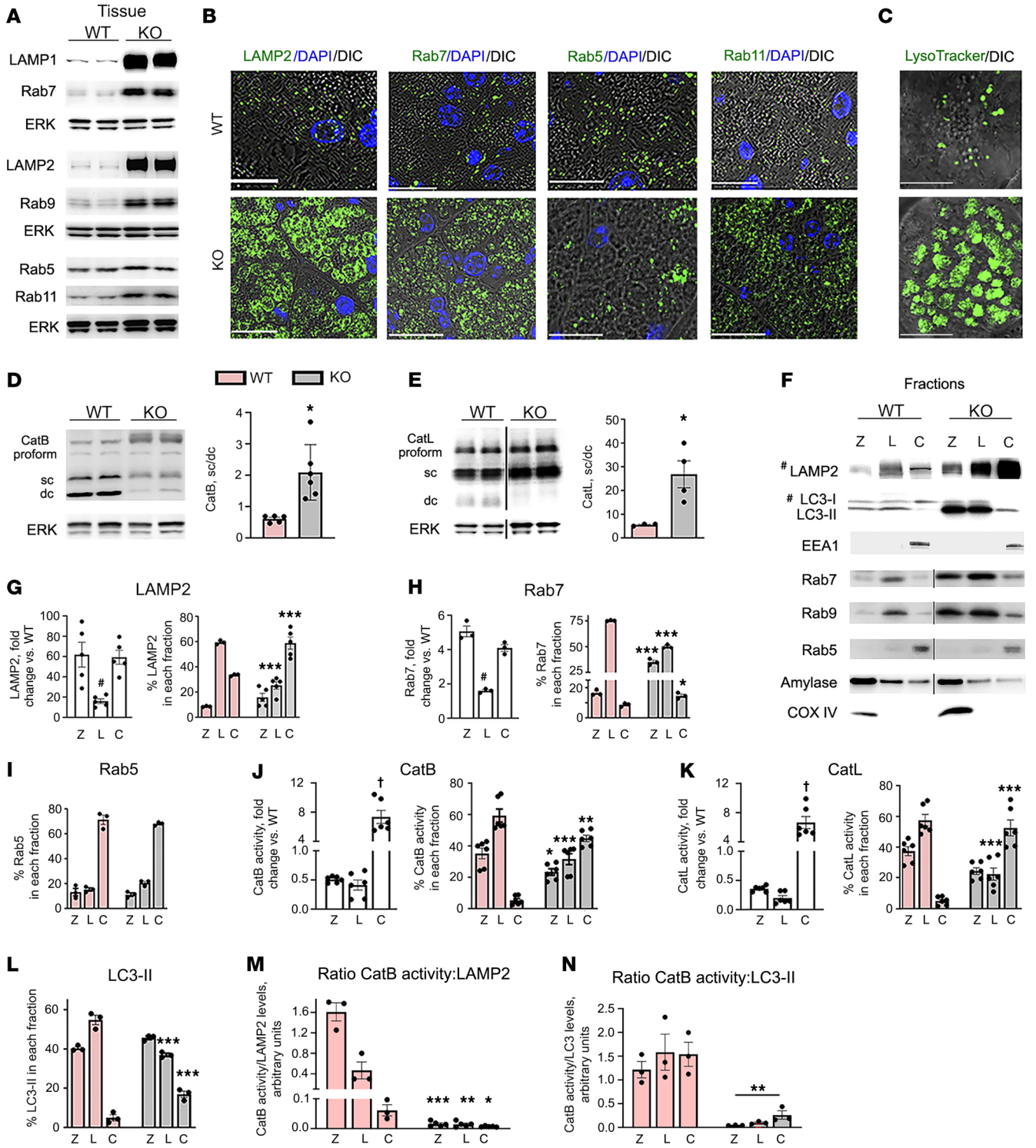


**Figure 1. *Gnptab* ablation perturbs the endolysosomal system in the exocrine pancreas.** Characteristics of the endolysosomal system were measured in WT and *Gnptab*$^{-/-}$ (KO) pancreatic (**A**, **B**, **D**, and **E**) tissue, (**C**) acinar cells, and (**F**–**N**) subcellular fractions. (**A** and **D**–**F**) IB analysis of organellar markers/mediators. In this and other figures, ERK1/2 or GAPDH is the loading control; each lane on tissue IB represents an individual mouse; black line (as in **F**) indicates lanes are on the same gel but not contiguous. Ub, ubiquitylated proteins. (**B**) Immunofluorescence analysis of indicated proteins. In this and other figures, nuclei are stained with DAPI (or NucRed); DIC denotes differential interference contrast microscopy, displaying zymogen granule area in acinar cells. Scale bars: 10 μm. (**C**) Acidic organelles stained using LysoTracker. (**D** and **E**) IB showing CatB and CatL pro-form, single-chain (sc), and mature/double-chain (dc) forms. (**F**–**N**) Protein levels of indicated markers/mediators (IB) and cathepsin activities (enzymatic assays) were measured in 3 subcellular pancreas fractions (see Methods): Z, enriched in zymogen granules; L, enriched in LE/Ly (in WT); and C, cytosol containing. The sum of band intensities for indicated proteins or cathepsin activities in all 3 fractions was taken as 100%. In **F**, # indicates that protein load of KO samples was 5 times less than WT. Values are mean ± SEM; each symbol represents an individual mouse ($n$ = 3–6 mice per condition). *$P < 0.05$, **$P < 0.01$, ***$P < 0.001$ vs. WT tissue (**D** and **E**) or corresponding WT fraction (**G**–**N**). $^{\#}P < 0.01$ (**G** and **H**) or $^{\dagger}P < 0.001$ (**J** and **K**) vs. the other two fractions. Significance was determined by 2-tailed Student's $t$ test (**D** and **E**) or 1-way ANOVA followed by Tukey's multiple comparison test (**G**–**N**).

a long-noted response of human and experimental pancreatitis (20, 21); we have shown that it is mediated by defective autophagy caused by lysosomal dysfunction (6, 22). Both *Gnptab*$^{-/-}$ pancreas and pancreatitis models display impaired activities and processing of lysosomal hydrolases. These similarities prompted us to investigate how the blockage of a key endolysosomal pathway affects the exocrine pancreas.

Here, we show that *Gnptab* ablation greatly perturbs the endolysosomal system and autophagy in the exocrine pancreas; in particular, it inhibited endocytic recycling, blocked autophagic flux, and stimulated autophagosome formation. But the key unexpected finding is that the M6P pathway is critical for maintaining exocrine pancreas cholesterol homeostasis. Cholesterol levels and its distribution among the plasma membrane and organelles (endolysosomes, ER, and mitochondria) regulate their stability and functions (23–26). Disordering of cholesterol metabolism should be particularly detrimental for acinar cell homeostasis and functions, as zymogen granule maturation, secretion, and membrane retrieval and recycling after exocytosis depend on efficient turnover of membranes' lipid components. However, essentially nothing is known about acinar cell cholesterol metabolism in healthy pancreas and its changes in experimental pancreatitis and human disease.

*Gnptab* ablation caused profound changes in acinar cell cholesterol synthesis, uptake, and subcellular distribution, resulting in accumulation of nonesterified cholesterol in late endosomes/lysosomes (LE/Ly) and autophagic vacuoles and its reduction in the plasma membrane. *Gnptab*$^{-/-}$ mice spontaneously developed pancreatitis with all major characteristics of human disease. We found similar dysregulation of cholesterol metabolism in experimental WT mouse and ex vivo pancreatitis models, while reducing acinar cell cholesterol overload alleviated disease. Importantly, we observed manifestations of disordered cholesterol metabolism in human pancreatitis. The results reveal the essential role of the M6P pathway in maintaining exocrine pancreas homeostasis and function, and implicate cholesterol disordering in the pathogenesis of pancreatitis.

## Results

### Blockage of the M6P pathway disrupts the endolysosomal system, autophagy, and endocytosis in the exocrine pancreas

*Gnptab ablation causes LE/Ly expansion and subcellular redistribution*. *Gnptab* ablation greatly increased pancreatic levels of LE/Ly markers LAMP1, LAMP2, Rab7, and Rab9 (Figure 1A). Their immunofluorescence (IF) pattern changed from small puncta in WT mice to large clumps of various shapes in *Gnptab*$^{-/-}$ (KO) pancreas (Figure 1B). The expansion and clumping of acidic organelles was also seen with LysoTracker (Figure 1C). In contrast, the levels of early (Rab5) and recycling (Rab11) endosomal markers increased only marginally (Figure 1A), and their IF staining (Figure 1B) remained dotted (although the size and cellular distribution of puncta changed somewhat).

Lysosomal hydrolases, such as cathepsins B and L (CatB and CatL), are synthesized as pro-proteins and undergo proteolytic processing first in endosomes, generating a partially processed single-chain (sc) form, and then in lysosomes where at acidic pH they mature into the fully processed, active double-chain (dc) form (27). *Gnptab* deficiency compromised cathepsins' maturation, as evidenced by increased amounts of the pro-form and 3- to 4-fold increases in sc/dc ratios for both CatB and CatL (Figure 1, D and E). Reduced sc-to-dc conversion in KO pancreas was also observed for CatD (19). The inhibition of cathepsin processing/maturation indicates that the delivery of these proteases to LE/Ly in pancreas, indeed, depends on the M6P pathway, the involvement of which is organ and cell specific (19, 28).

Of note, the pronounced reduction in the levels of the fully mature dc form (Figure 1, D and E) did not abrogate CatB and CatL activities (Figure 1, J and K), indicating that the partially processed sc form possesses considerable catalytic activity.

To further analyze the effect of *Gnptab* ablation on the endolysosomal system, we used (Figure 1, F–N) commonly applied pancreatic tissue fractionation (6, 29–31) to generate 3 subcellular fractions: Z (1300*g* pellet), L (12,000*g* pellet), and C (12,000*g* supernatant). In WT pancreas the heavier fraction Z was enriched in zymogen granule markers (i.e., amylase) and contained mitochondria (COX IV), whereas the cytosol-containing fraction C was selective for the markers of early endosomes (EE), Rab5 and EEA1 (Figure 1F; see also ref. 6). Fraction L in WT was enriched in LE/Ly (LAMP2, Rab7, and Rab9) and exhibited the highest CatB and CatL activities (Figure 1, F–K). This subcellular distribution is characteristic of healthy cells in which the level of lysosomal proteolytic activity correlates with the amount of LE/Ly.

*Gnptab* ablation altered the subcellular distribution of LE/Ly and cathepsin activities in the pancreas. LAMP2, Rab7, and Rab9 increased in all 3 fractions, but fraction L exhibited the smallest increase, resulting in LE/Ly shift away from fraction L to Z and C (Figure 1, G and H). In contrast, the distribution of EE (Rab5 and EEA1), zymogen granules (amylase), and mitochondria (COX IV) did not significantly change (Figure 1, F and I). CatB and CatL activities increased in fraction C but decreased by half in fractions Z and L, altering cathepsins' subcellular distribution profile (Figure 1, J and K). Thus, the substantial LE/Ly expansion in KO pancreas was not matched/counterbalanced by corresponding increases in cathepsin activity (as would be expected in cells with competent LE/Ly), which was evidenced by a greater than 100-fold decrease in the ratio of CatB activity to LAMP2 level across the fractions (Figure 1M).

The data on subcellular redistribution indicate structural changes in the exocrine pancreas endolysosomal system. *Gnptab* ablation caused an imbalance between LE/Ly expansion and their reduced proteolytic capacity; one underlying mechanism could be impaired processing/maturation of cathepsins.

### *Gnptab* ablation stimulates autophagosome formation and blocks autophagic flux

*Gnptab* ablation greatly increased pancreatic levels of LC3-II (Figure 1F and Figure 2, A–D), a marker of autophagic vacuoles (also observed in ref. 19). LC3-II levels in KO pancreas increased in all 3 fractions, but more significantly in C, resulting in subcellular redistribution of LC3-II (Figure 1, F and L). The CatB activity/LC3-II ratio markedly decreased (Figure 1N), especially in fractions Z and L, similar to that for LAMP2 (Figure 1M).

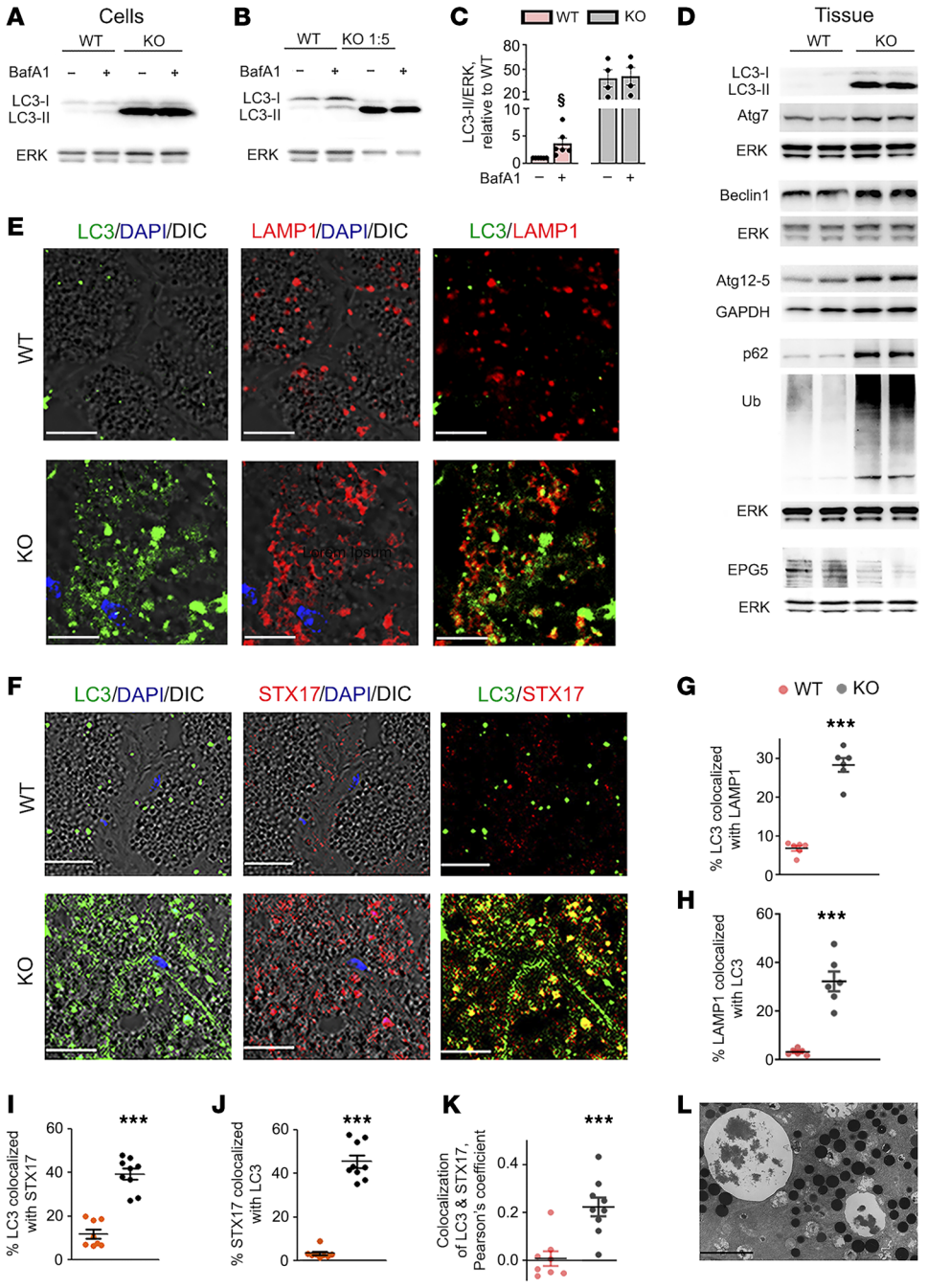


**Figure 2. *Gnptab* ablation stimulates autophagosome formation and blocks autophagic flux in pancreatic acinar cells.** Parameters of autophagy were measured in WT and *Gnptab*$^{-/-}$ (KO) pancreatic (**A**–**C**) acinar cells and (**D**–**L**) tissue. (**A**–**C**) Acinar cells incubated for 30 minutes with and without bafilomycin A1 (BafA1; 20 nM); LC3-II band intensity was quantified by densitometry, normalized to ERK in the same sample, and LC3-II/ERK ratios further normalized to untreated WT cells (control). Values are mean ± SEM; each symbol represents an individual cell preparation ($n$ = 4–6 per condition). $^{\S}P < 0.05$; paired 2-tailed Student's $t$ test. (**D**) IB analysis of autophagic markers/mediators. Ub, ubiquitylated proteins. (**E**–**K**) Immunofluorescence colocalization analysis for LC3 and LAMP1 (**E**, **G**, and **H**), and LC3 and Stx17 (**F** and **I**–**K**) in WT and KO pancreas. In this and other figures, colocalization was quantified with Volocity software using Manders-Costes (percentage colocalization) and Pearson's coefficients. Values are mean ± SEM; each symbol corresponds to 20 to 30 cells in a different field ($n$ = 6–9 fields from 3 mice per condition). $^{***}P < 0.001$ vs. WT; 2-tailed Student's $t$ test. (**L**). EM showing abnormally large autolysosomes with partially degraded material in pancreas of KO mice. Scale bars: 10 μm (**E** and **F**) and 3 μm (**L**).

To further assess the effects of *Gnptab* KO on autophagy, we performed autophagic flux analysis by measuring changes in LC3-II in acinar cells incubated with and without the lysosomal v-ATPase inhibitor, bafilomycin A1 (BafA1) (Figure 2, A–C). The number of autophagic vacuoles in a cell is a net balance between autophagosome formation and their degradation through autophagic flux. Thus, the increase in LC3-II observed in KO pancreas (Figure 1F and Figure 2D; see also Supplemental Figure 6G; supplemental material available online with this article; https://doi.org/10.1172/JCI146870DS1) could have resulted from both induction of autophagosome formation and the inhibition of flux. BafA1 blocks lysosomal/autophagic degradation but does not affect autophagosome formation; thus, in the presence of BafA1 any difference in cellular LC3-II levels between 2 conditions (e.g., KO vs. WT) is due solely to changes in autophagosome formation (31, 32). In the presence of BafA1, LC3-II levels were approximately 11-fold higher in KO compared with WT (Figure 2, A–C), indicating strong induction of autophagosome formation in *Gnptab*$^{-/-}$ acinar cells.

On the other hand, the magnitude of LC3-II increase elicited by BafA1 in a given condition (e.g., WT cells) reflects the efficiency of autophagic degradation in this condition; the greater the LC3-II increase, the greater was the contribution of autophagic flux abrogated by BafA1 (31, 32). In WT acinar cells, BafA1 increased LC3-II approximately 4-fold (Figure 2C), reflecting efficient basal autophagic flux, the blockage of which by BafA1 caused accumulation of LC3-positive autophagic vacuoles (31). Remarkably, in KO cells BafA1 elicited no increase in LC3-II

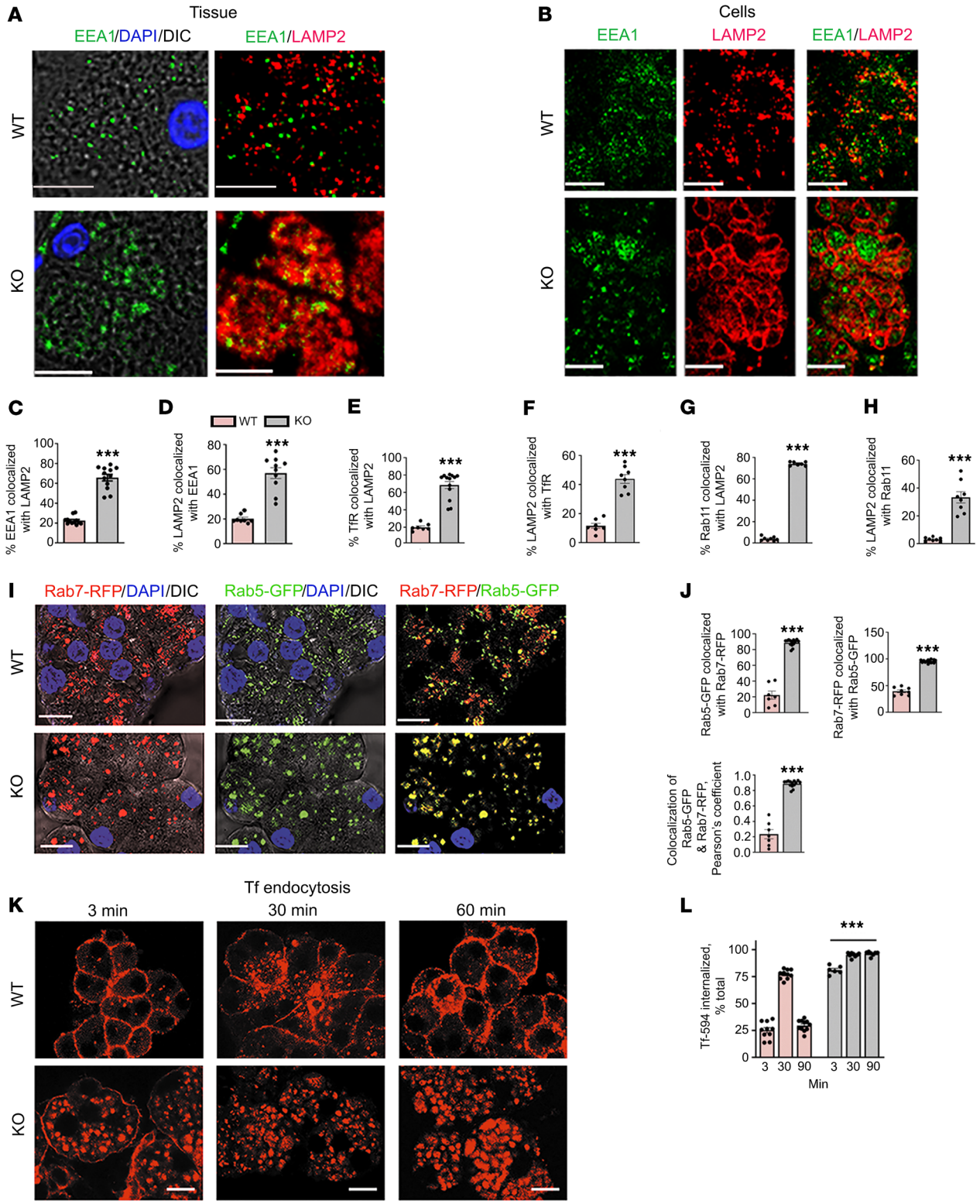


**Figure 3. *Gnptab* ablation impairs early-to-late endosome maturation and endocytic recycling.** Immunofluorescence analysis of markers of early (EEA1, TfR, Rab5), recycling (Rab11), and late (LAMP2, Rab7) endosomes in pancreatic (**A** and **C**–**H**) tissue and (**B**, **I**, and **J**) acinar cells (see also images in the Supplemental Figure 1). In **I** and **J**, acinar cells were transduced with both CellLight Rab5-GFP and Rab7-RFP. Quantitative colocalization analysis for indicated proteins was done as detailed in Figure 2. Values are mean ± SEM; each symbol corresponds to 20 to 30 cells in a different field ($n$ = 7–14 fields from 3 to 4 mice or cell preparations per condition). ***$P < 0.001$ vs. WT; 2-tailed Student's $t$ test. (**K** and **L**) To measure transferrin (Tf) endocytosis, acinar cells were loaded with Tf-594 at 0°C, transferred to 37°C, incubated for the indicated times, and visualized with confocal microscopy. Internalized Tf-594 was quantified using Volocity software. Values are mean ± SEM; each symbol corresponds to 10 to 15 cells in a different field ($n$ = 6–11 fields from 3 WT and 3 KO cell preparations). ***$P < 0.001$ vs. corresponding WT condition; 1-way ANOVA followed by Tukey's multiple comparison test. Scale bars: 10 μm.

(Figure 2, A–C), indicating a complete block of autophagic degradation and demonstrating a critical role of the M6P pathway in maintaining efficient pancreatic autophagy. Together, the block of autophagic flux and rise in autophagosome formation increased the basal LC3-II level in *Gnptab*$^{-/-}$ cells approximately 37-fold compared with WT (Figure 2C).

In accord with these results, we observed marked increases in pancreatic levels of not only LC3-II but also the autophagy substrate p62/SQSTM1 and ubiquitylated proteins (Figure 2D), corroborating impaired autophagic degradation (32). Other mediators of autophagosome formation, Beclin1/ATG6, ATG5 (i.e., ATG12-ATG5 conjugate), and ATG7, were moderately elevated (Figure 2D). *Gnptab* ablation did not block autophagosome fusion with lysosomes, as evidenced by dramatic increases in LC3-II colocalization with LAMP1 and acquisition of STX17, a key mediator of this fusion, into LC3-positive puncta in KO acinar cells (Figure 2, E–K). Also, numerous enlarged autolysosomes containing partially degraded material were seen on electron micrographs of KO pancreas (Figure 2L and ref. 19).

We found a marked decrease in KO pancreas of EPG5 (Figure 2D), a protein that promotes autolysosomal proteolytic activity and genetic deletion of which causes formation of nondegradative autolysosomes (33). Together with LC3-II subcellular redistribution and the markedly decreased CatB activity/LC3-II ratio (Figure 1, L and N), these data support the notion of an imbalance between increased autophagosome formation and low proteolytic activity in LC3-positive autophagic vacuoles.

Thus, *Gnptab* ablation stimulates acinar cell autophagy but blocks its completion (autophagic flux), resulting in accumulation of autolysosomes with low degradative capacity.

*Gnptab KO impairs EE-to-LE maturation and endocytic recycling.* Transport of endocytosed cargos to the lysosome depends on EE maturation into LE (34, 35), which involves transient formation of hybrid compartments containing markers of both EE (e.g., Rab5) and LE (Rab7, LAMP2). In WT pancreas, only approximately 20% of the EE markers EEA1 and transferrin receptor (TfR), and approximately 4% of the recycling endosomal marker Rab11 colocalized with LAMP2; these values increased up to approximately 70% in KO pancreas (Figure 3, A–H, and Supplemental Figure 1), indicating impaired EE maturation. IF images (Figure 3, A and B, and Supplemental Figure 1) showed EE markers trapped within large organelles decorated with ring-like LAMP2, most clearly seen in KO acinar cell preparations (Figure 3B). Further, *Gnptab* deficiency increased Rab5/Rab7 colocalization several-fold in acinar cells double-transduced with Rab5a-GFP and Rab7a-RFP (Figure 3, I and J). Thus, EE maturation is impaired in the *Gnptab*$^{-/-}$ pancreas, causing accumulation of hybrid endosomes that bear markers of both EE and LE.

The iron-carrying protein transferrin (Tf) is endocytosed upon binding its receptor (TfR), releases iron, and is recycled back to the plasma membrane; this process serves as an archetypical model of receptor-mediated cargo delivery (35). We measured endocytosis of fluorescently labeled Tf (Figure 3, K and L), the uptake of which was initiated by transferring acinar cells from 0°C to 37°C. Immediately (3 minutes) after initiating endocytosis in WT cells, the labeled Tf was mostly (~75%) present on the plasma membrane; after 30 minutes, the Tf-TfR complex accumulated in EE, and by 90 minutes it largely returned to the cell surface. By contrast, in *Gnptab*$^{-/-}$ cells Tf internalization was already prominent at 3 minutes (suggesting enhanced Tf endocytosis) but there was no recycling back to the plasma membrane at 90 minutes (Figure 3, K and L). The results indicate inhibition of endocytic recycling in KO acinar cells; one reason for this could be impaired EE-to-LE maturation.

### The M6P pathway is critical for maintaining pancreatic cholesterol homeostasis

*Gnptab KO perturbs pancreatic lipids.* Numerous lipid-like inclusions were seen on electron micrographs of KO pancreas, suggesting that the M6P pathway modulates acinar cell lipid metabolism (Supplemental Figure 2A). Whereas WT acinar cells contained few lipid droplets, blockage of autophagy by *Gnptab* ablation or in mice with pancreas-specific knockout of ATG5 (*Atg5*$^{\Delta pan}$), a key mediator of autophagosome formation, increased neutral lipids in the pancreas approximately 4-fold (Supplemental Figure 2, B and C), as measured with the neutral lipid stain BODIPY 493/503 (36). Similarly, BafA1 treatment of WT acinar cells increased BODIPY staining approximately 3-fold, and there was no additional effect of BafA1 on the greatly elevated BODIPY staining in *Gnptab*$^{-/-}$ cells (Supplemental Figure 2, D and E). (Note that the pattern of BODIPY staining was different in BafA1-treated WT vs. KO cells.) These results reveal a key role of autophagy (lipophagy; ref. 37) in maintaining neutral lipid metabolism in the exocrine pancreas.

Accumulation of neutral lipids in KO pancreas was associated with a decrease in perilipins (Supplemental Figure 2, F and G), proteins essential for the integrity of lipid droplet membranes (38). We also found increased BODIPY colocalization with both LC3 and LAMP1 (Supplemental Figure 3). Thus, *Gnptab* ablation caused accumulation of neutral lipids in LE/Ly and autophagic vacuoles, while decreasing their cytosolic storage.

*Gnptab KO disrupts cholesterol metabolism in the exocrine pancreas. Gnptab* ablation increased both the total and nonesterified (free) cholesterol content in pancreas 3- to 4-fold (Figure 4, A and B), while it did not significantly elevate triglyceride and free fatty acid levels (Figure 4, C and D). Corroborating these data, LC-MS/GC-MS analysis showed several-fold increases in major cholesterol esters in KO pancreas, but not in other classes of lipids tested (Figure 4E). We further found activation of several mechanisms that increase free cholesterol: the expression of genes mediating cholesterol synthesis (Figure 4F), activity of lysosomal acid lipase (LAL) (Figure 4G), the level of low-density lipoprotein receptor (LDLR) (Figure 4H), and uptake of exogenous LDL (Figure 4I).

In WT acinar cells (Figure 4, J–L, and Supplemental Figure 4) approximately 40% of filipin, a fluorescent probe for free cholesterol, localized to the plasma membrane (based on its marker cadherin), and another approximately 40% to zymogen granules (based on amylase), a distribution pattern similar to that of other secretory cells (23). Only 5% to 10% of the filipin probe colocalized with markers of LE/Ly (LAMP2, NPC1), EE (EEA1), or autophagic vacuoles (LC3; Figure 4, M–R, and Supplemental Figure 5). By contrast, in *Gnptab*$^{-/-}$ acinar cells approximately 84% of filipin accumulated in organelles wrapped with LAMP2-positive membranes (Figure 4, O and P); a similar colocalization pattern was seen for filipin and NPC1 on IF images (Supplemental Figure 5A).

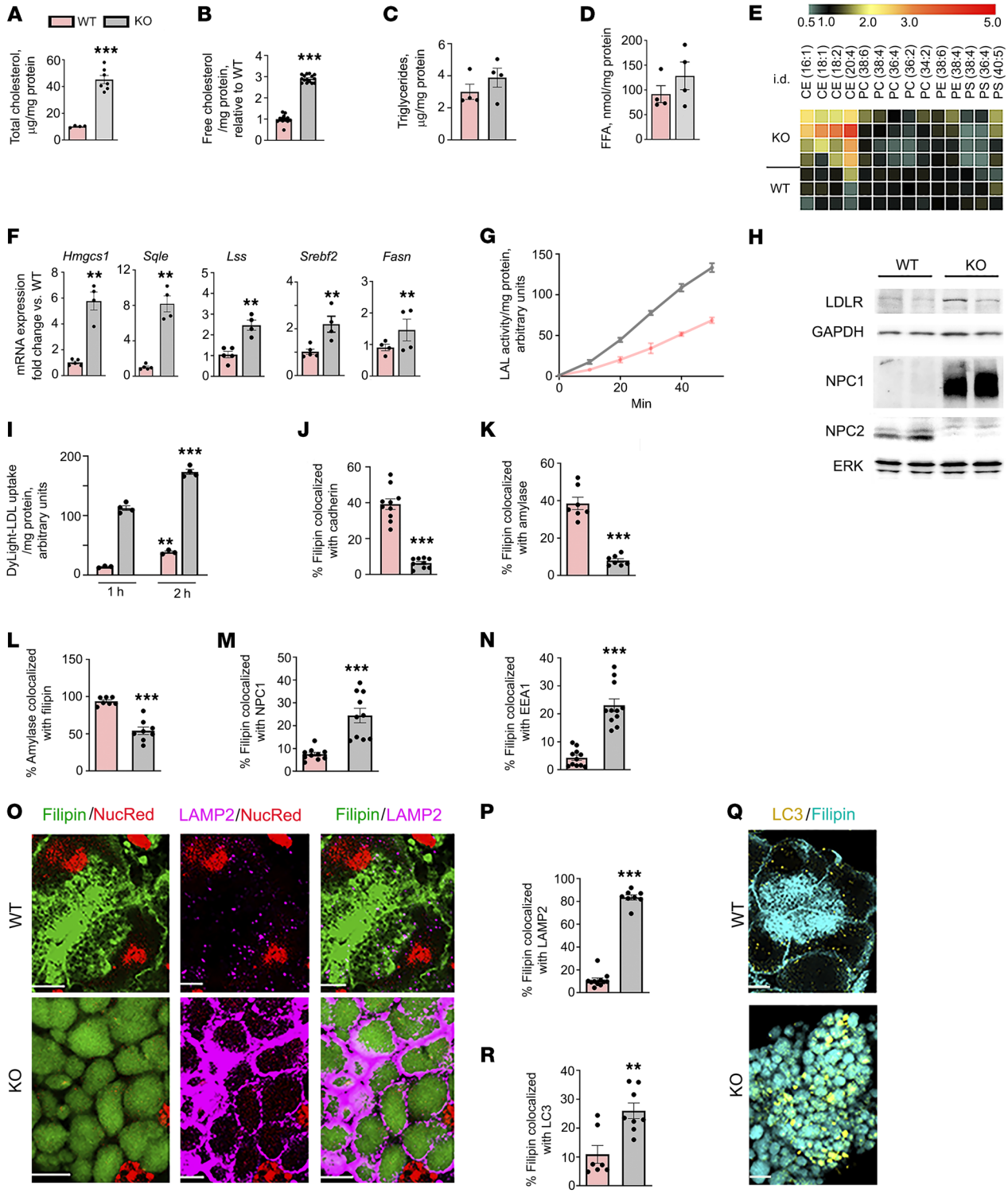


**Figure 4. *Gnptab* ablation disrupts cholesterol metabolism in the exocrine pancreas.** Parameters of cholesterol metabolism were measured in pancreatic (**A**–**H**) tissue and (**I**–**R**) acinar cells. (**A**–**D**) Pancreatic contents of total and nonesterified (free) cholesterol, triglycerides, and free fatty acids (FFA); each symbol represents an individual mouse. (**E**) Heatmap of lipid species of indicated cholesterol esters (CE), phosphatidylcholine (PC), phosphatidylethanolamine (PE), and phosphatidylserine (PS), measured with LC-MS/GC-MS. Each row represents an individual mouse. (**F**) mRNA expression of proteins regulating the synthesis of cholesterol and fatty acids was measured by qPCR; each symbol represents an individual mouse. Values were normalized to the housekeeping gene *Rplp0/36B4* and are expressed relative to WT. (**G**) Lysosomal acid lipase (LAL) activity was measured with a fluorogenic assay. (**H**) IB analysis of NPC1, NPC2, and LDLR. (**I**) LDL uptake was measured with DyLight550-LDL probe; each symbol represents a different cell preparation. (**J**–**R**) Colocalization of the free-cholesterol probe filipin with indicated proteins (see also images in Supplemental Figures 4 and 5) was quantified using confocal microscopy and the Manders-Costes coefficient. Each symbol corresponds to 10 to 15 cells in a different field ($n$ = 5–11 fields from 3 WT and 3 KO cell preparations). Values are mean ± SEM from 3 to 7 (**A** and **C**–**G**) or 14 to 15 (**B**) mice of each strain, or from 3 to 4 acinar cell preparations per condition (**I** and **J**–**R**). $^{**}P < 0.01$, $^{***}P < 0.001$ vs. WT; 2-tailed Student's $t$ test. Scale bars: 10 µm.

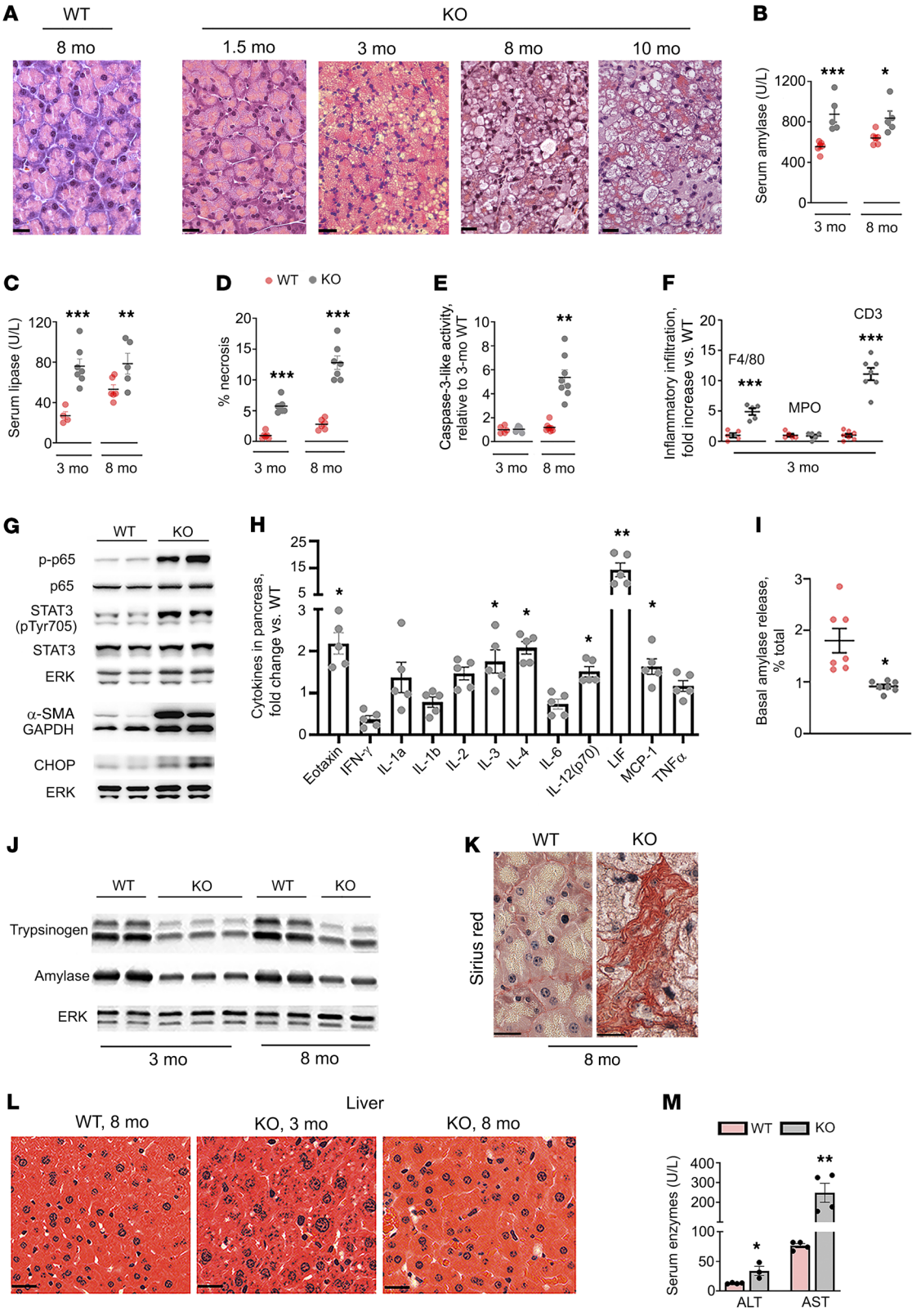


**Figure 5. *Gnptab*$^{-/-}$ mice develop pancreatitis.** Parameters of pancreas (**A**–**K**) and liver (**L** and **M**) damage in KO mice of different age (3 months old [mo] if not specified). (**A** and **L**) Histopathologic changes (H&E staining). (**B**–**F**) Pancreatitis responses. In **F**, macrophage (F4/80), neutrophil (MPO; myeloperoxidase), and T cell (CD3) infiltration in pancreas was quantified by IHC (see images in Supplemental Figure 8). (**G** and **J**) IB analysis of total and phosphorylated (active) NF-κB (p-p65/RelA) and STAT3 (p-Tyr705-STAT3), and other proteins in pancreas. (**H**) Proinflammatory cytokines and chemokines were measured (per mg protein) with Luminex Multiplexing analyzer. (**I**) The basal/unstimulated amylase secretion was measured as a percentage of its total acinar cell content (see Methods). (**K**) Sirius red staining showing pancreatic fibrosis. (**M**) Serum markers of liver injury. Values are mean ± SEM from 3 to 8 mice of each strain; each symbol represents an individual mouse or cell preparation. $^{*}P < 0.05$, $^{**}P < 0.01$, $^{***}P < 0.001$ vs. WT; 2-tailed Student's *t* test. Scale bars: 10 μm.

Free cholesterol colocalization with EEA1 and LC3 also increased several-fold in KO cells, whereas it markedly decreased in both the plasma membrane and zymogen granules (Figure 4, J–N, Q, and R, and Supplemental Figures 4 and 5).

NPC1 and NPC2 proteins mediate transport of endocytosed cholesterol through LE/Ly (39). Similar to other LE/Ly membrane proteins (LAMP2, Rab7), NPC1 levels greatly increased in KO pancreas (Figure 4H and Supplemental Figure 6). By contrast, we observed a marked decrease in NPC2 level in KO pancreas (Figure 4H and Supplemental Figure 6) — in accord with the findings that, unlike NPC1, NPC2 targeting to LE/Ly is strictly dependent on the M6P pathway (28, 40).

Thus, blockage of the M6P pathway causes profound disruption of cholesterol homeostasis in the exocrine pancreas. This was manifested by a marked decrease in plasma membrane cholesterol, critical for maintaining conformation of ion channels and receptors and cell viability (23–26); reduction of cholesterol in membranes of zymogen granules (where it is necessary for regulated secretion; ref. 41); and cholesterol accumulation in LE/Ly and autolysosomes, reducing its availability for the cell's needs. Likely as a compensatory response, *Gnptab*$^{-/-}$ acinar cells upregulated both cholesterol synthesis and uptake. Notably, we did not observe any significant changes in serum cholesterol levels in *Gnptab*$^{-/-}$ mice.

*Gnptab KO effects on the endolysosomal system and cholesterol are organ specific*. *Gnptab*$^{-/-}$ livers exhibited impaired CatB processing (manifested by a decrease in its dc form) and reduced NPC2 levels (Supplemental Figure 6, A, E, and F), as seen in KO pancreas. However, there was no upregulation of LAMP2, Rab7, NPC1, LC3-II, and p62, and no decrease in EPG5 in KO liver (Supplemental Figure 6, A–D, G, and H). *Gnptab* deficiency did not change liver triglycerides, free fatty acids, or total and free cholesterol (Supplemental Figure 6I). Perilipin 2 (PLIN2) levels decreased in KO liver, but there was little or no reduction in PLIN3 and PLIN5 (Supplemental Figure 6, A and J) as seen in the pancreas (Supplemental Figure 2, F and G). *Gnptab* ablation did not increase EEA1 colocalization with LAMP2 in the liver (Supplemental Figure 7A) or BODIPY colocalization with LAMP2, indicative of neutral lipid accumulation in LE/Ly (Supplemental Figure 7B).

Thus, overall, blockage of the M6P pathway did not significantly perturb the endolysosomal system and neutral lipids in the liver. In contrast to the pancreas, *Gnptab* deficiency in the liver did not cause LE/Ly expansion, accumulation of hybrid endosomes, or impaired autophagy.

#### *Gnptab*$^{-/-}$ mice develop pancreatitis

Acinar cell vacuolization, observed with light microscopy, was evident in 1.5-month-old KO mice, and vacuole size and pancreas disorganization increased with age (Figure 5A). In addition to histopathologic changes, by 3 months *Gnptab*$^{-/-}$ mice developed signature responses of pancreatitis (1, 3): increased levels of serum amylase and lipase, inflammation, parenchymal necrosis, and increased caspase-3–like activity indicative of apoptosis (Figure 5, B–F); as well as an upsurge in intrapancreatic trypsin activity (see below). Inflammatory infiltration in the pancreas was driven by macrophages and T cells, and not neutrophils (Figure 5F and Supplemental Figure 8), which is a pattern characteristic of a chronic inflammatory response. We observed activation (i.e., phosphorylation) of the proinflammatory transcription factors NF-κB and STAT3 in KO pancreas (Figure 5G) and increased levels of cytokines and chemokines, such as LIF, IL-3, IL-4, and CCL11/eotaxin-1 (Figure 5H). Pancreatic levels of CHOP, an ER stress marker and cell death mediator, markedly increased (Figure 5G); those of amylase and trypsinogen decreased (Figure 5J), indicating exocrine pancreas atrophy. Basal (unstimulated) amylase secretion was inhibited in KO acinar cells (Figure 5I). Pancreatic fibrosis was evidenced by upregulation of α-SMA, a marker of activated stellate cells (Figure 5G), and by Sirius red staining (Figure 5K). In contrast, *Gnptab*$^{-/-}$ liver displayed no vacuolization or other histopathologic changes, and the serum markers of liver damage, alanine (ALT) and aspartate (AST) aminotransferases, were only mildly elevated (Figure 5, L and M).

The results show that blockage of the M6P pathway causes spontaneous pancreatitis in mice.

#### Trypsin activity cholesterol-dependently increases in *Gnptab*$^{-/-}$ pancreas

*Gnptab* deficiency greatly increased intrapancreatic trypsin activity (Figure 6A), also evidenced by increased levels of trypsinogen activation peptide (TAP) (Figure 6, E and F), an oligopeptide cleaved off trypsinogen during its conversion to active trypsin (6, 42). The inappropriate, intra-acinar trypsinogen activation is a hallmark of pancreatitis but its mechanism, and the site(s) where it occurs, remain obscure (5, 43). In experimental pancreatitis it is mediated by CatB (6, 43, 44), and, indeed, the CatB inhibitor CA-074Me reduced trypsin activity in *Gnptab*$^{-/-}$ acinar cells by half (Figure 6B). In normal secretory cells, the nascent immature secretory granules, due to imperfect sorting, have an admixture of lysosomal enzyme precursors, although the majority of their content are secretory proteins. During granule maturation, hydrolases are removed through an M6P receptor–mediated mechanism (discussed in ref. 5). Because in KO pancreas cathepsins lack the M6P tag, this mechanism is compromised and one might presume that CatB is retained (i.e., mis-sorted) in mature zymogen granules (19) and activates trypsinogen there. However, CatB colocalization with trypsinogen did not increase in KO pancreas (Figure 6, C and D), arguing against the predominance of this mechanism. (Note that CatB colocalization with trypsinogen is fairly robust in WT acinar cells, Pearson's coefficient; Figure 6D).

Instead, *Gnptab* ablation greatly increased TAP colocalization with LAMP2 and LC3 (Figure 6, E–H). Further, BafA1 reduced trypsin activity in KO acinar cells by half (Figure 6B). These results indicate trypsin localization in acidic CatB-containing organelles, as also supported by the subcellular fractionation data. In WT pancreas, trypsinogen mostly localized to fraction Z (enriched in zymogen granules) and the bulk of trypsin activity was in the Z and L fractions (Figure 6, I–K). *Gnptab* deficiency did not change the subcellular distribution of trypsinogen (Figure 6, I and J; as also seen for amylase, another zymogen granule protein, Figure 1F). However, the percentage of trypsin activity in fraction Z decreased in KO pancreas, while its largest (~4.7-fold) increase was in fraction C (Figure 6, K and L), which contained EEA1 and Rab5 and harbored large increases in LC3-II and LAMP2 levels and CatB activity (Figure 1, F, G, I, J, and L).

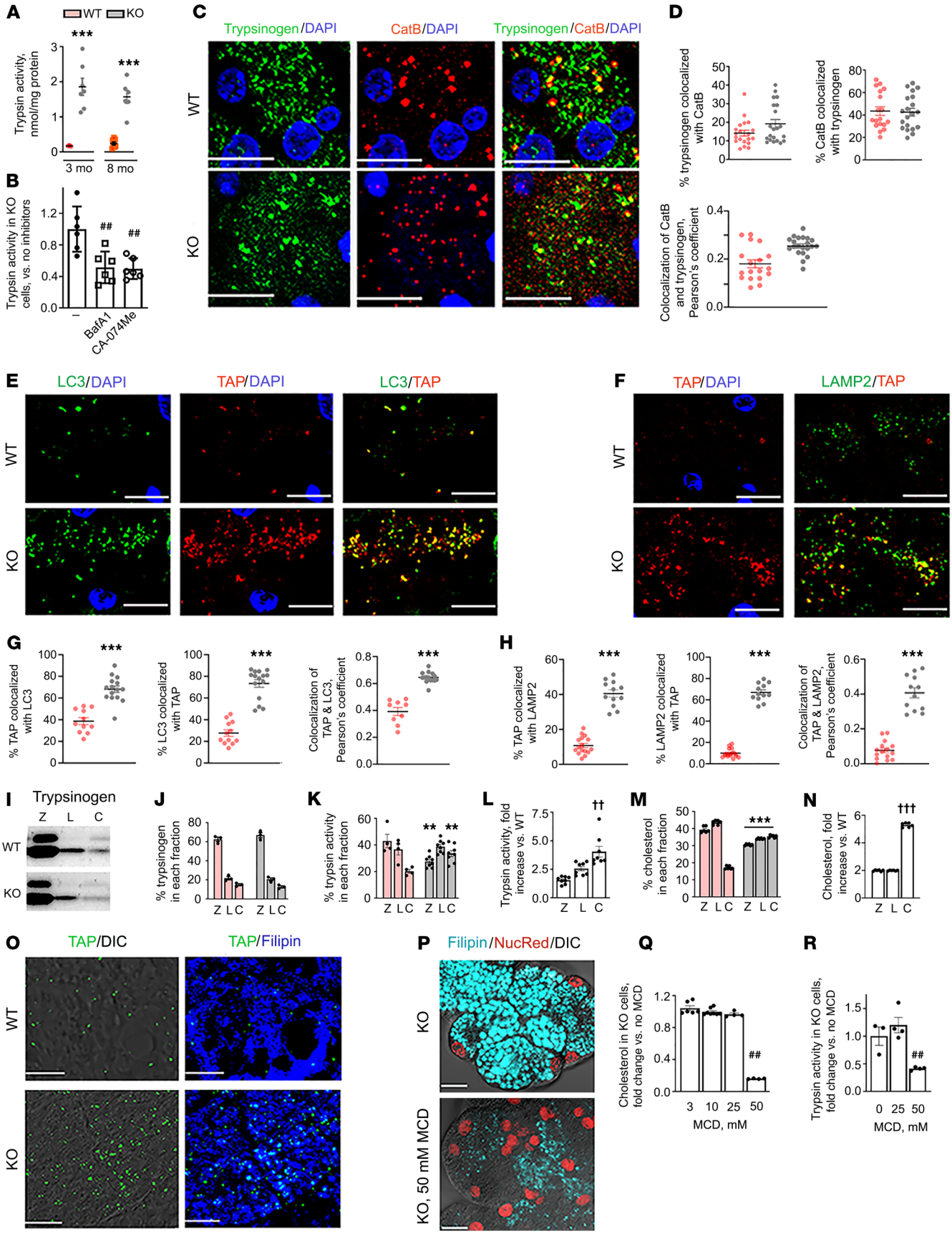
A
WT
KO
***
***
Trypsin activity, nmol/mg protein
3 mo
8 mo
B
Trypsin activity in KO cells, vs. no inhibitors
##
##
–
BafA1
CA-074Me
C
Trypsinogen/DAPI
CatB/DAPI
Trypsinogen/CatB/DAPI
WT
KO
D
% trypsinogen colocalized with CatB
% CatB colocalized with trypsinogen
Colocalization of CatB and trypsinogen, Pearson's coefficient
E
LC3/DAPI
TAP/DAPI
LC3/TAP
WT
KO
F
TAP/DAPI
LAMP2/TAP
WT
KO
G
% TAP colocalized with LC3
% LC3 colocalized with TAP
Colocalization of TAP & LC3, Pearson's coefficient
***
H
% TAP colocalized with LAMP2
% LAMP2 colocalized with TAP
Colocalization of TAP & LAMP2, Pearson's coefficient
***
I
Trypsinogen
Z L C
WT
KO
J
% trypsinogen in each fraction
Z L C Z L C
K
% trypsin activity in each fraction
**
**
Z L C Z L C
L
Trypsin activity, fold increase vs. WT
††
Z L C
M
% cholesterol in each fraction
***
Z L C Z L C
N
Cholesterol, fold increase vs. WT
†††
Z L C
O
TAP/DIC
TAP/Filipin
WT
KO
P
Filipin/NucRed/DIC
KO
KO, 50 mM MCD
Q
Cholesterol in KO cells, fold change vs. no MCD
##
3 10 25 50
MCD, mM
R
Trypsin activity in KO cells, fold change vs. no MCD
##
0 25 50
MCD, mM

**Figure 6. Mechanisms mediating increased trypsin activity in *Gnptab*$^{-/-}$ pancreas.** Trypsin activity and its regulation were analyzed in pancreatic (**A**, **C**, and **D**) tissue, (**B** and **P**–**R**) acinar cells, (**E**–**H** and **O**) lobules, and (**I**–**N**) subcellular fractions. In **B**, acinar cells were incubated for 3 hours without and with 20 nM BafA1 or 50 μM CatB inhibitor CA-074Me; in **P**–**R**, with the cholesterol chelator methyl-β-cyclodextrin (MCD) at the indicated concentrations. In **E**–**H**, pancreatic lobules were double stained for TAP and LC3 or LAMP2; in **O**, for TAP and filipin. Quantitative colocalization analysis was done as detailed in Figure 2. Each symbol in **A**, **B**, **J**–**N**, **Q**, and **R** represents an individual mouse or cell preparation ($n$ = 3–8 per condition). Each symbol in **D**, **G**, and **H** corresponds to 20 to 30 cells in a different field ($n$ = 9–20 fields from 3 WT and 3 KO mice or lobule preparations). Values are mean ± SEM. $^{**}P < 0.01$, $^{***}P < 0.001$ vs. WT tissue/lobules (**A**, **G**, and **H**) or corresponding WT subcellular fraction (**K** and **M**). $^{\#\#}P < 0.01$ vs. no inhibitors (**B**) or MCD (**Q** and **R**). $^{\dagger\dagger}P < 0.01$, $^{\dagger\dagger\dagger}P < 0.001$ vs. the other two fractions (**L** and **N**). Significance was determined by 2-tailed Student's $t$ test (**A**, **G**, and **H**) or 1-way ANOVA followed by Tukey's multiple comparison test (**B**, **K**–**N**, **Q**, and **R**). Scale bars: 10 μm.

The subcellular distribution of trypsin activity in KO pancreas was similar to that of cholesterol, in that the greatest increase in both was in fraction C (Figure 6, K–N). TAP colocalized with filipin-positive structures (Figure 6O); furthermore, reducing cholesterol content with its chelator, methyl-β-cyclodextrin (MCD), greatly decreased trypsin activity in KO cells (Figure 6, P–R). Of note, *Gnptab*$^{-/-}$ acinar cells were highly resistant to MCD, with the cholesterol-reducing effect evident only at 50 mM MCD (Figure 6, Q and R) instead of the usual 1 to 5 mM (45).

The results show that the M6P pathway regulates intrapancreatic trypsin activity in a cholesterol-dependent manner, and implicate endosomal and autophagic compartments — but not zymogen granules — as the sites of trypsinogen activation in *Gnptab*$^{-/-}$ acinar cells. Our data are consistent with the notion that the colocalization organelles may originate from fusion of trypsinogen-containing autophagosomes with endosomes (such as the hybrid EE/LE) in which the partially processed (sc form) CatB is active; these amphisomes may subsequently fuse with lysosomes. The observed increases in both trypsin activity and cholesterol in fraction C could be explained by accumulation of low-density, cholesterol-rich autophagic vacuoles in this fraction. The mechanisms through which cholesterol regulates trypsinogen activation in pancreatitis remain to be determined.

### *Gnptab* ablation causes mitochondrial dysfunction in the pancreas

Mitochondrial dysfunction drives pancreatitis in experimental mouse and cellular models and is associated with human disease (5, 46–48). However, the role of the endolysosomal system, in particular the M6P pathway, in pancreatic mitochondrial homeostasis has not been explored. We found pronounced mitochondrial dysfunction in *Gnptab*$^{-/-}$ pancreas, manifested by reduced enzymatic activities of electron transport chain (ETC) complexes II and IV (Figure 7A); decreased rates of basal, ATP-linked, and maximal oxygen respiration (oxygen consumption rate, OCR) (Figure 7, B and C); and a marked decrease in pancreatic ATP level (Figure 7E). In WT pancreatic mitochondria, ADP-stimulated ATP synthesis caused a decrease in mitochondrial membrane potential (ΔΨm), which returned to basal levels after ADP was converted to ATP (Figure 7D). In contrast, the ΔΨm recovery following ADP addition was greatly inhibited in *Gnptab*$^{-/-}$ mitochondria (Figure 7D), indicating impaired ATP synthase function (46). Levels of Fis1, a protein involved in mitochondrial fragmentation, and Parkin, a mitophagy mediator (49), increased in KO pancreas (Figure 7F). The increase in mitochondrial fragmentation was evidenced by IF of the mitochondria-resident proteins Tom20 and VDAC, which showed a disjoined and mostly circular pattern in KO pancreas, in contrast with the interconnected tubular mitochondrial network in WT (Figure 7G). Of note, *Gnptab* ablation did not decrease immunoblot (IB) levels of mitochondrial markers, i.e., the outer mitochondrial membrane protein Tom70 and the inner mitochondrial membrane protein COX IV (Figure 7H), indicating no decrease in the amount of mitochondria in KO pancreas.

Collectively, the results show a major role of the M6P pathway in maintaining acinar cell mitochondrial functions.

Some of the mitochondrial defects in *Gnptab*$^{-/-}$ pancreas could be the result of perturbed lipid metabolism. Specifically, ATP production in WT acinar cells is mediated by free fatty acid oxidation, as evidenced by inhibition of both basal and ATP-linked OCR with etomoxir (Figure 7I), a β-oxidation inhibitor (50). In KO acinar cells, the respiration rates were much lower and not significantly reduced by etomoxir (Figure 7I). One reason for this could be the approximately 2-fold decrease in free fatty acid content in KO pancreatic mitochondria (Figure 7J), likely a consequence of reduced availability of lipid droplets (Supplemental Figures 2 and 3) that deliver free fatty acids to mitochondria (51). With LC-MS/GC-MS, we also showed increased levels of long-chain acylcarnitines in KO pancreas (Figure 7K), an indication of impaired β-oxidation (52, 53).

We further found that the cholesterol content of *Gnptab*$^{-/-}$ pancreatic mitochondria increased approximately 2.5-fold (Figure 7M), which is damaging for mitochondrial functions (24, 54). Elevated cholesterol interferes with assembly of ETC complexes and thus could be responsible for their reduced activity and dysregulation of mitochondrial ATP synthesis (Figure 7, A–E). One likely mechanism mediating mitochondrial cholesterol overload in KO pancreas is the increase in MLN64/STARD3 protein (Figure 7L), which belongs to the STARD family of lipid transfer proteins that transport cholesterol directly from LE/Ly to mitochondria. This pathway is activated in conditions of inhibited cholesterol egress from lysosomes, and STARD protein levels increase in response to a defective supply of cholesterol to mitochondria via normal routes (24, 55, 56). A similar paradoxical effect of mitochondrial cholesterol overload despite disrupted cholesterol turnover, as well as increased levels of STARD protein, was observed in Niemann-Pick type C (NPC) disease models (55).

Notably, in contrast to pancreas, *Gnptab* deficiency in liver mitochondria did not alter ETC complex activities, the ADP-mediated ΔΨm response, cholesterol content, or MLN64 levels (Figure 7, N–Q).

### Cholesterol metabolism is disrupted in experimental pancreatitis

Lipidomic and enzymatic analyses showed increases in pancreatic total cholesterol in 3 dissimilar acute pancreatitis (AP) models induced in WT mice using L-arginine (Arg-AP), the CCK-8 ortholog cerulein (CER-AP), or choline deficient, ethionine-supplemented diet (CDE-AP) (Figure 8, A and B). Similarly, cholesterol content increased in mouse (Figure 8C) and, notably, human (Figure 8D) acinar cells stimulated with supramaximal (100 nM) CCK-8 (CCK-AP) or carbachol (ex vivo AP models). Physiologic doses

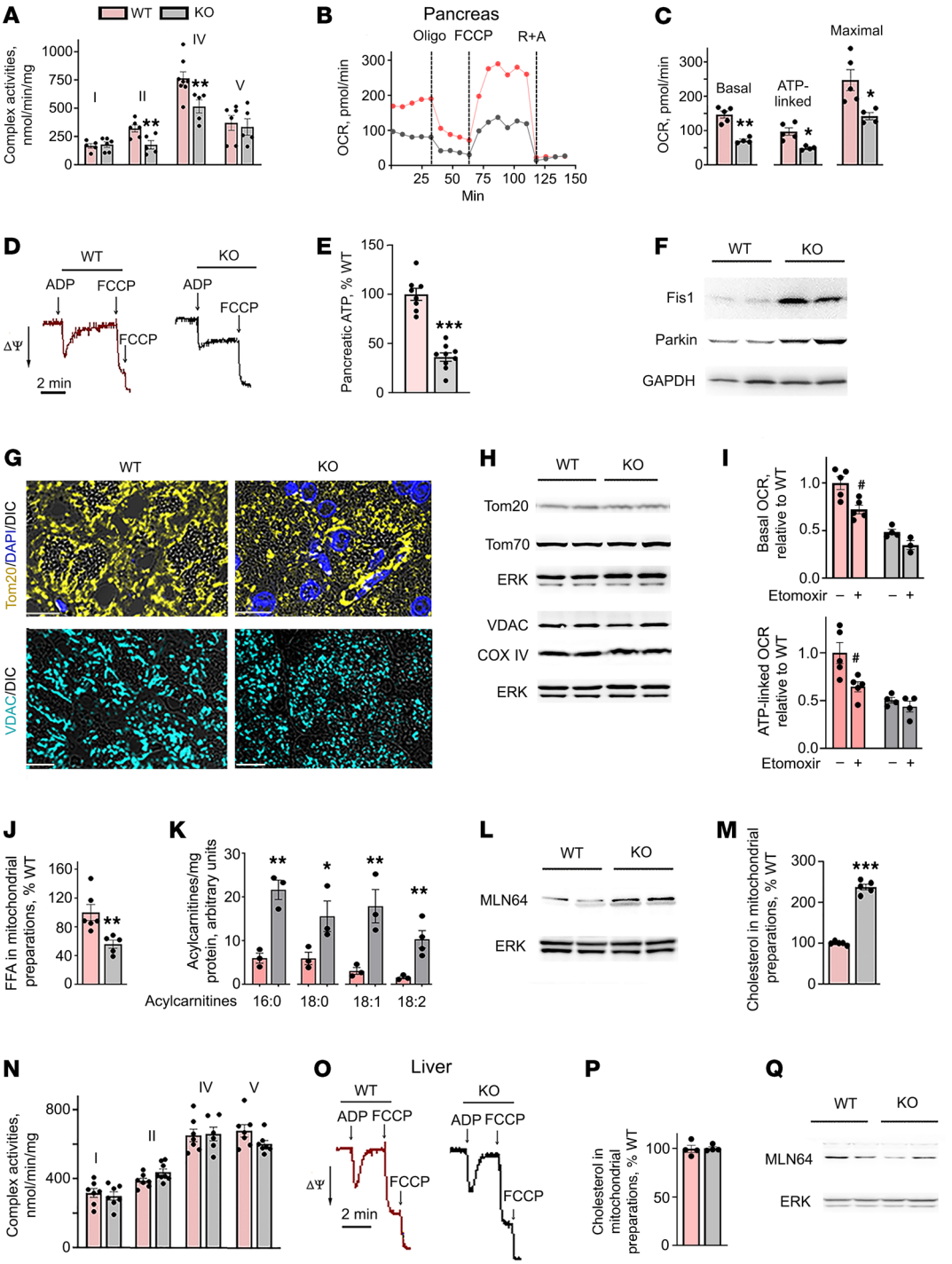


**Figure 7. *Gnptab* ablation causes mitochondrial dysfunction in the pancreas.** Mitochondrial functional parameters were measured in mitochondria isolated from pancreas (**A**, **D**, **J**, and **M**) or liver (**N**–**P**), in acinar cells (**B**, **C**, and **I**), and pancreatic (**E**–**H**, **K**, and **L**) and liver (**Q**) tissues of WT and KO mice. (**A** and **N**) Activities of mitochondrial ETC complexes I, II, IV, and V. (**B**, **C**, and **I**) Acinar cell oxygen consumption rates (OCR), reflecting mitochondrial OXPHOS, were measured in basal conditions and after treatment with the β-oxidation inhibitor etomoxir (40 μM), and normalized to total protein in the sample. (**B**) Representative OCR tracings in acinar cell suspension subjected to consecutive injections of the ATP synthase inhibitor oligomycin (Oligo; 3 μM), protonophore FCCP (2.7 μM), and mitochondrial uncouplers rotenone plus antimycin A (R+A, 5 μM each; to correct for nonmitochondrial respiration). (**C** and **I**) ATP-linked respiration was calculated as the difference between basal OCR and that in Oligo-treated cells; the maximal OCR was obtained in FCCP-treated cells. (**D** and **O**) Mitochondrial membrane potential (ΔΨm) was measured with a tetraphenyl phosphonium ion ($TPP^+$) electrode. FCCP (5 μM) was added to completely dissipate ΔΨm. (**E**) ATP was measured in pancreatic tissue homogenate with luciferin-luciferase assay. (**F**, **H**, **L**, and **Q**) IB analysis of the mitochondrial fission factor Fis1 and mitophagy mediator Parkin (**F**), mitochondrial markers (**H**), and MLN64/STARD3 protein (**L** and **Q**) that mediates cholesterol transfer from LE/Ly directly to mitochondria. (**G**) Mitochondrial fragmentation was assessed by changes in Tom20 or VDAC immunostaining pattern, from an interconnected tubular mitochondrial network in WT to a predominantly disjoined/circular one in KO pancreas. Scale bars: 10 μm. (**J**, **M**, and **P**) Free fatty acid (FFA) and cholesterol contents of isolated pancreatic or liver mitochondria. (**K**) Long-chain acylcarnitines were measured with LC-MS/GC-MS. Values are mean ± SEM; each symbol represents an individual mouse, or cell or mitochondria preparation ($n$ = 3–8 per condition). $^*P < 0.05$, $^{**}P < 0.01$, $^{***}P < 0.001$ vs. the same parameter in WT. $^{\#}P < 0.05$ vs. the same condition without etomoxir (**I**). Significance was determined by 2-tailed Student's $t$ test.

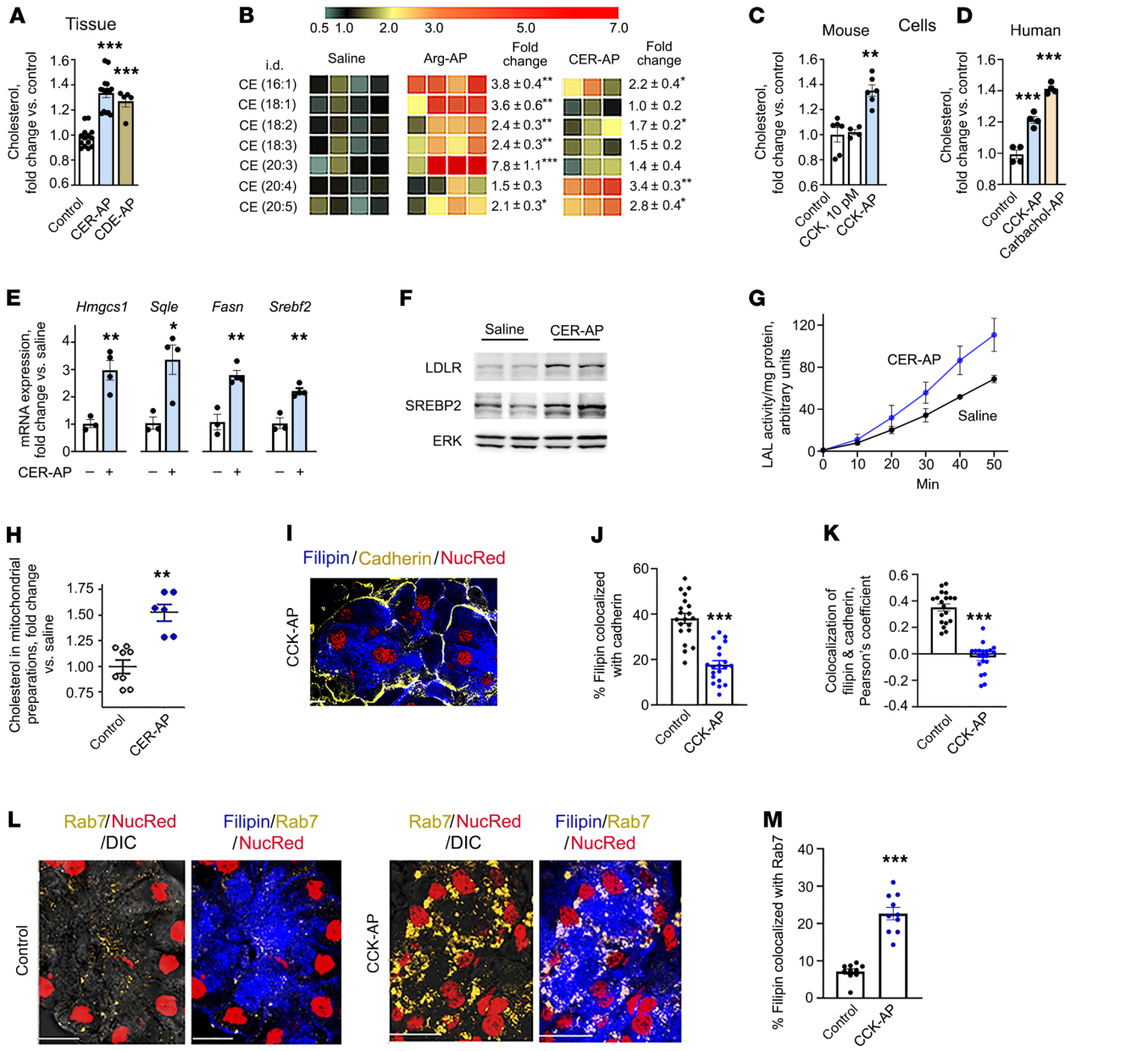


**Figure 8. Derangement of cholesterol metabolism in experimental pancreatitis.** Characteristics of cholesterol metabolism were measured, as detailed in Figure 4, in pancreas of WT mice subjected to pancreatitis induced with cerulein (CER-AP), L-arginine (Arg-AP), or CDE diet (CDE-AP) (**A**, **B**, and **E**–**G**); ex vivo pancreatitis induced in WT mouse (**C** and **I**–**M**) or human acinar cells (**D**) with 100 nM CCK (CCK-AP) or 1 mM carbachol; and isolated pancreatic mitochondria (**H**). (**B**) Cholesterol ester (CE) heatmap; each column represents an individual mouse. (**F**) IB analysis of the indicated proteins. (**G**) LAL activity was measured by a fluorogenic assay ($n$ = 6 mice per condition). (**H**) Cholesterol content was measured by enzymatic assay. (**I**–**M**) Filipin colocalization with indicated proteins was quantified as detailed in Figure 2. Each symbol in **A**, **C**–**E**, and **H** represents an individual mouse, or cell or mitochondria preparation ($n$ = 3–15 per condition). Each symbol in **J**, **K**, and **M** corresponds to 20–30 cells in a different field ($n$ = 10–20 fields from 3 cell preparations per condition). Values are mean ± SEM. $^*P < 0.05$, $^{**}P < 0.01$, $^{***}P < 0.001$ vs. the same parameter in control/untreated pancreas, acinar cells or isolated mitochondria. Significance was determined by 2-tailed Student's $t$ test (**B**, **E**, **H**, **J**, **K**, and **M**) or 1-way ANOVA followed by Tukey's multiple comparison test (**A**, **C**, and **D**). Scale bars: 10 μm.

of CCK (10 pM) or carbachol did not alter total cholesterol in acinar cells, and pancreatic triglycerides were unchanged in CER-AP (Figure 8C, and data not shown).

We examined in more detail the changes in acinar cell cholesterol metabolism in CER/CCK-AP, the most widely used animal and ex vivo pancreatitis model (3). Similar to *Gnptab*$^{-/-}$ (Figure 4), in WT mice with CER-AP we found upregulation of pancreatic mRNA expression for enzymes mediating cholesterol synthesis (Figure 8E), increased protein levels of LDLR and SREBP2 (Figure 8F) and LAL activity (Figure 8G), and elevated mitochondrial cholesterol (Figure 8H). Further, the plasma membrane free cholesterol (i.e., filipin colocalization with cadherin) markedly decreased in the ex vivo CCK-AP model, concomitant with its accumulation in Rab7-positive LE/Ly (Figure 8, I–M). These changes are similar to those seen in KO pancreas. As in *Gnptab*$^{-/-}$ mice, serum cholesterol levels did not change in CER-AP.

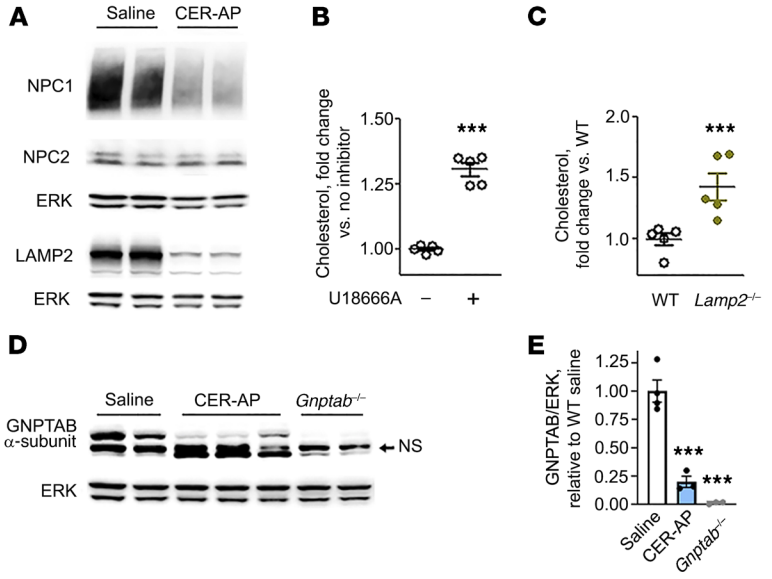


**Figure 9. Cerulein pancreatitis decreases pancreatic levels of GNPTAB and mediators of cholesterol trafficking through LE/Ly.** (**A**, **D**, and **E**) IB analysis of the indicated proteins in pancreas of WT mice subjected to CER-AP and in *Gnptab*$^{-/-}$ mice. NS, nonspecific band. (**B** and **C**) Cholesterol content was measured in pancreas of (**B**) WT mice that received daily i.p. injections of the NPC1 inhibitor U18666A (10 mg/kg) or vehicle for 15 days and (**C**) *Lamp2*$^{-/-}$ mice. Each symbol in **B**, **C**, and **E** represents an individual mouse. Values are mean ± SEM from 3 to 5 mice per condition. ***$P < 0.001$ vs. the same parameter in WT control/untreated or saline-treated mice. Significance was determined by 2-tailed Student's *t* test (**B** and **C**) or 1-way ANOVA followed by Tukey's multiple comparison test (**E**).

We tested whether experimental pancreatitis altered the NPC2/NPC1 pathway that mediates cholesterol transport through LE/Ly (39). Unlike *Gnptab*$^{-/-}$ pancreas, there was no change in NPC2 levels, but pancreatic NPC1 greatly decreased in CER-AP (Figure 9A). Administration of U18666A, a selective NPC1 inhibitor (57), elevated cholesterol content in WT mouse pancreas (Figure 9B). We found a similar increase in pancreatic cholesterol in mice deficient in LAMP2 (Figure 9C), another LE/Ly protein mediating cholesterol trafficking (58). Of note, pancreatic LAMP2 levels greatly decrease in various pancreatitis models, including CER-AP (Figure 9A), as well as in human disease (8). The results in U18666A-treated WT mice and in *Lamp2*$^{-/-}$ mice (Figure 9, B and C) confirm the role of NPC1 and LAMP2 in regulating pancreatic cholesterol.

We found that CER-AP elicited an approximately 5-fold decrease in pancreatic GNPTAB α-subunit protein level (Figure 9, D and E). This effect could mediate alterations in cholesterol metabolism that we observed in experimental pancreatitis. The fact that the NPC2 level was not reduced in CER-AP (Figure 9A), despite a marked decrease in GNPTAB α-subunit, may indicate increased NPC2 synthesis, blocked excretion, or a threshold pattern of its regulation by the M6P pathway in the pancreas.

#### Cholesterol normalization ameliorates experimental pancreatitis

We found (Figure 10, A–F) that, as in *Gnptab*$^{-/-}$ mice, cholesterol regulates trypsinogen activation in WT experimental pancreatitis. Cholesterol overload (using cholesterol-loaded MCD) increased basal trypsin activity in WT acinar cells (Figure 10, A and B), whereas depleting cholesterol with MCD reduced CCK-induced trypsinogen activation in ex vivo pancreatitis (Figure 10, C and D). In accord with these data, T0901317, which promotes cholesterol efflux by activating the LXR receptor (59, 60), and simvastatin, an inhibitor of cholesterol synthesis, ameliorated experimental pancreatitis in WT mouse and ex vivo models. Both compounds eliminated pancreatitis-induced increases in total cholesterol and trypsin activity (Figure 10, E and F). Of note, the same T0901317 or simvastatin treatments of *Gnptab*$^{-/-}$ mice, even for 3 weeks, failed to decrease pancreatic total cholesterol levels, confirming the resistance of KO acinar cells to reducing cholesterol overload (see Figure 6, Q and R). T0901317 and simvastatin improved pancreas histopathology in CER-AP (Figure 10G and Supplemental Figure 9A); reduced accumulation of LC3-II, p62, and ubiquitylated proteins, indicating more efficient autophagy; and decreased CHOP levels, indicating lower ER stress (Figure 10, H and I, and Supplemental Figure 9B). T0901317 and simvastatin also normalized mitochondrial fragmentation, as assessed by Tom20 IF (Figure 10J), and abrogated the CER-induced increase in MLN64 (Supplemental Figure 9B). In addition to improved histopathology, simvastatin also ameliorated other pancreatitis responses (Supplemental Figure 9C).

To examine the effect of disrupted cholesterol turnover, we incubated WT acinar cells with LDL-cholesterol in the presence and absence of the NPC1 inhibitor U18666A. U18666A caused cholesterol accumulation in LE/Ly (filipin staining; Figure 10K), resulting in impaired autophagy (manifested by concomitant accumulation of LC3-II and ubiquitylated proteins) and increases in CHOP and Parkin (Figure 10L). Similarly, mice that received U18666A and thus had elevated total cholesterol (Figure 9B) exhibited pancreas damage manifested by increased acinar cell vacuolization, necrosis (up to ~20%), and inflammation (Figure 10M), and accumulation of LC3-II, p62, and ubiquitylated proteins (Figure 10N).

Taken together, amelioration of experimental pancreatitis with T0901317 and simvastatin, and the detrimental effects of U18666A suggest that disordered acinar cell cholesterol metabolism mediates impaired autophagy, ER stress, and other pathologies of pancreatitis.

#### Human pancreatitis displays signs of disordered acinar cell cholesterol homeostasis

Using IF analysis of deidentified tissue sections from patients with and without pancreatitis, we found an approximately 3-fold increase in pancreatic HMG-CoA reductase, and dramatic decreases in NPC1 and GNPTAB levels in pancreatitis tissues (Fig-

ure 11). The specificity of the anti–GNPTAB α-subunit antibody was confirmed by IB analysis (Figure 9D). None of the patients, except one, had pancreatic adenocarcinoma (Supplemental Table 1). Remarkably, both the direction and magnitude of the changes we observed in human disease are similar to those presented above in experimental models of pancreatitis.

## Discussion

Our study in *Gnptab*$^{-/-}$ mice reveals that an efficient endolysosomal system and autophagy, and in particular the M6P pathway, are critical for maintaining cholesterol metabolism in the exocrine pancreas. We find that cholesterol derangement mediates experimental pancreatitis pathologies, and that the human disease displays signs of impaired acinar cell cholesterol homeostasis. Our results show a central role of the M6P pathway in key exocrine pancreas cellular processes: autophagy, endocytosis, and mitochondrial functions; and establish *Gnptab*$^{-/-}$ mice as a genetic model of pancreatitis.

*Gnptab* ablation perturbed the acinar cell endolysosomal system, manifested by underprocessing of cathepsins and the expansion of LE/Ly that was not matched by an increase in cathepsins' activities, resulting in diminished lysosomal proteolytic capacity. We found impaired EE-to-LE maturation causing accumulation of hybrid endosomes. In turn, the major functions of the endolysosomal system, autophagy and endocytic recycling, were severely compromised. *Gnptab* deficiency both stimulated autophagosome formation in acinar cells and blocked autophagic flux, causing accumulation of large nondegradative autolysosomes. Deranged endocytosis was manifested by increased Tf internalization and inhibition of its recycling.

We find that *Gnptab* deficiency greatly perturbed many aspects of cholesterol metabolism, as reflected by several-fold increases in total and free cholesterol, upregulated expression of proteins mediating cholesterol synthesis, and increased LDL uptake. In contrast to WT, free cholesterol in KO acinar cells accumulated in large LAMP2-positive structures occupying the bulk of the cytoplasm. This was associated with a deleterious cholesterol reduction in the plasma membrane and zymogen granules. Of note, the distribution of cholesterol among subcellular membranes is highly uneven. In healthy cells, most of cellular cholesterol is localized to the plasma membrane to maintain its proper fluidity and rigidity, as well as to secretory granules; by contrast, mitochondria and lysosomes contain minor amounts of cholesterol (23–26).

The results indicate that two major mechanisms mediating these effects are defective cholesterol trafficking through LE/Ly and blockage of autophagic flux. We find that autophagy/lipophagy plays a key role in lipid droplet degradation in normal pancreas, and its impairment results in accumulation of neutral lipids in nondegradative autolysosomes, making free cholesterol unavailable for the cell's needs. In response, *Gnptab*$^{-/-}$ acinar cells upregulate both cholesterol synthesis and uptake, which exacerbates cholesterol derangement by further increasing its content.

This paradoxical response, and other alterations in cholesterol metabolism in *Gnptab*$^{-/-}$ pancreas, resemble those observed in the lysosomal storage disease NPC. The disease is caused by mutations in NPC2 or NPC1, proteins that mediate cholesterol transport through LE/Ly (39, 58). NPC2 lacking the M6P recognition marker fails to reach lysosomes and is secreted (28, 40). Congruently, NPC2 levels greatly decreased in *Gnptab*$^{-/-}$ pancreas, likely mediating cholesterol accumulation in LE/Ly. Mouse NPC models showed structural alterations in pancreatic acinar cells, e.g., lipid accumulation in lysosomes and a reduction in secretory granules (61, 62); pancreas damage in NPC patients has not been examined. However, there have been no reports of pancreatitis in NPC patients (or mouse models), suggesting that NPC2 deficiency by itself is insufficient to cause disease.

*Gnptab* ablation caused pancreatic mitochondrial failure evidenced by decreased ETC complex activities and oxidative phosphorylation (OXPHOS), impaired ATP synthesis, and increased mitochondrial fragmentation. The results reveal a critical role for the M6P pathway in maintaining mitochondrial functions in the pancreas. Our data implicate several mechanisms mediating mitochondrial failure in *Gnptab*$^{-/-}$ pancreas. One is the blockage of autophagy/mitophagy, causing accumulation of dysfunctional mitochondria. Another is perturbed neutral lipid metabolism, resulting in impaired β-oxidation and increased mitochondrial cholesterol. The latter can impede ETC complex formation and ATP synthesis (24, 54).

In contrast to the pancreas, *Gnptab*$^{-/-}$ livers did not exhibit pathologic changes in the endolysosomal system, autophagy, mitochondrial functions, or cholesterol content. This is consistent with a previous study showing organ-specific effects of *Gnptab* ablation (19), likely due to varying contributions of compensatory, M6P-independent mechanisms of acid hydrolases' targeting to endolysosomes (28). However, some effects were shared by KO pancreas and liver, such as the markedly decreased levels of perilipin 2, a critical lipid droplet protein (38), revealing a role for the M6P pathway in lipid droplet homeostasis.

In humans, mutations in the *GNPTAB* gene cause mucolipidosis type II (MLII), a fatal disease characterized by damage to mesenchymal cells (i.e., skin fibroblasts) and skeletal and other abnormalities (15, 16, 61). Some, but not all, of these defects are observed in mice with an MLII patient's *GNPTAB* mutation knocked in (15). *Gnptab*$^{-/-}$ mice, in which the gene is completely ablated by retroviral gene trapping, do not replicate MLII pathology (18, 19, 28); in particular, there is not much damage to fibroblasts. However, these mice provide a valuable tool to study the roles and mechanisms of endolysosomal and autophagy pathways in secretory cells (this study and ref. 19). Pancreatitis has not been reported in MLII patients, but an autopsy study of juvenile MLII patient (63) found extensive damage (i.e., massive vacuolization) in several secretory glands including exocrine pancreas. The remarkably variable sensitivity of different organs and cell types to defects in GNPTAB, observed in both MLII patients and mouse models (15, 16, 19, 28), reflects the contribution of alternative and compensatory, M6P-independent mechanisms (as well as interspecies differences). The difference between the effects of a mutated (15) versus fully ablated *Gnptab* gene (this study and refs. 18, 19) may also indicate a role for protein-protein interactions involving GNPTAB, in addition to its enzymatic function. Of note, the ablation of the cation-independent M6P receptor in mice (64) caused much less pancreas damage than in *Gnptab*$^{-/-}$ (though it worsened experimental pancreatitis), possibly indicating a compensatory contribution of the second, cation-dependent, M6P receptor.

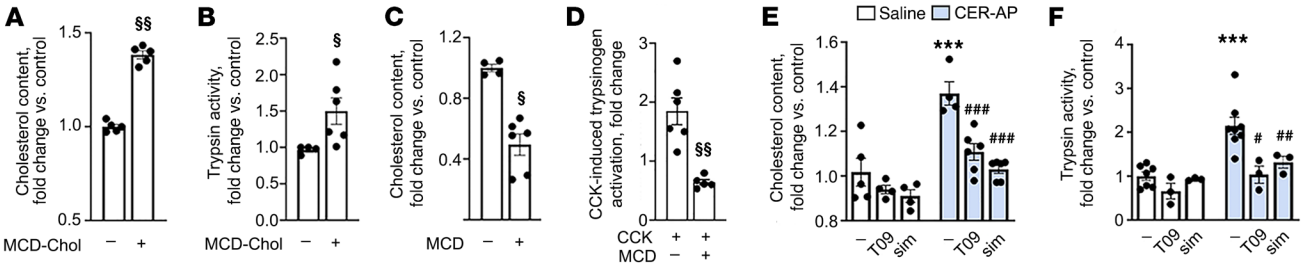


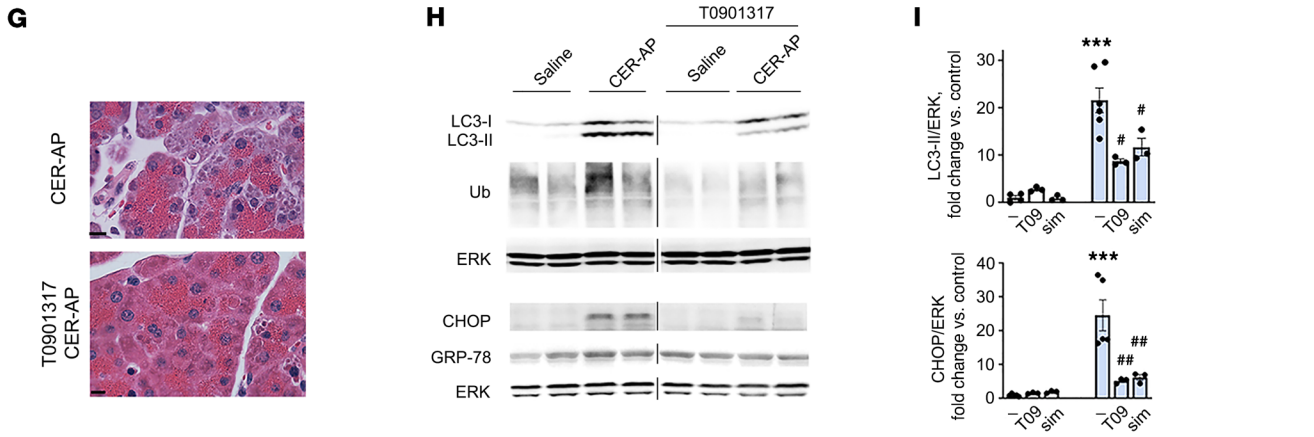


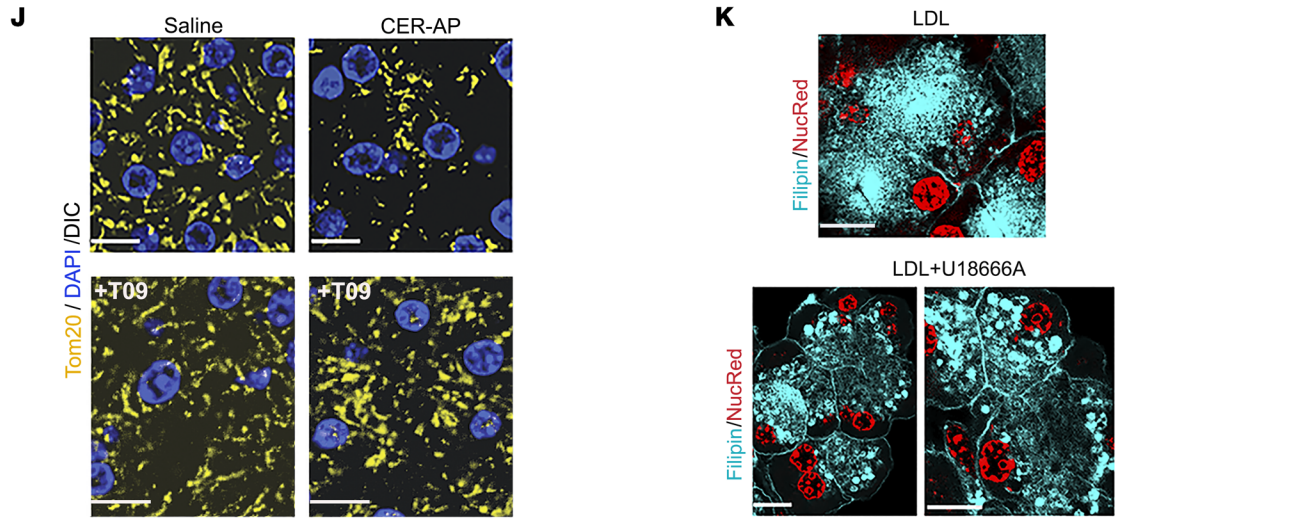


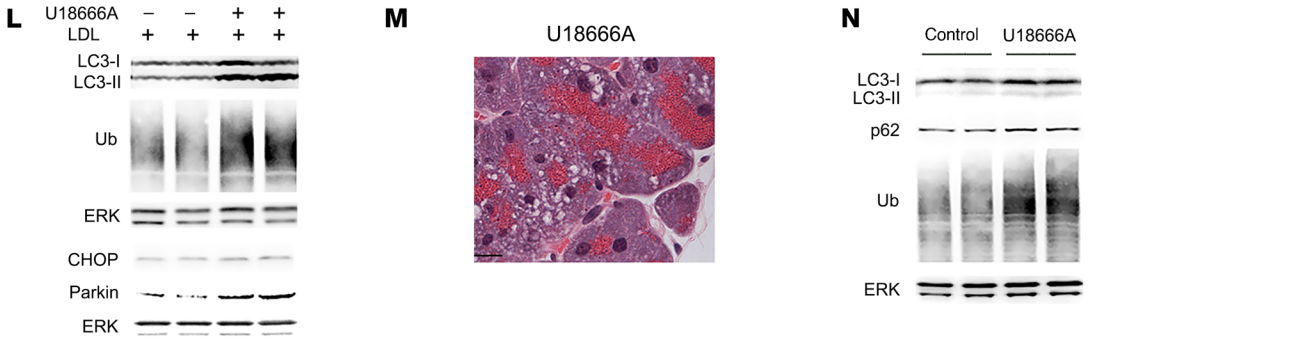



J Clin Invest. 2021;131(15):e146870 https://doi.org/10.1172/JCI146870

**Figure 10. Deranged cholesterol metabolism causes acinar cell damage, while its normalization ameliorates experimental pancreatitis.** (**A**–**D**) Cholesterol content and trypsin activity were measured (per mg protein) in WT mouse acinar cells incubated for 1 hour without and with methyl-β-cyclodextrin (MCD; 10 mM) or cholesterol-loaded MCD (MCD-Chol; 200 μg/mL), in the presence or absence of 100 nM CCK. Values are expressed relative to those in cells without MCD/MCD-Chol. (**E**–**J**) WT mice received daily i.p. injections of the LXR agonist T0901317 (T09), simvastatin (Sim; 20 mg/kg each), or vehicle. On day 4, mice were subjected to CER-AP and pancreata collected for analyses (see also Supplemental Figure 9). Cholesterol content (**E**), trypsin activity (**F**), and pancreas histopathology (H&E staining; **G**) were measured. (**H**, **I**, **L**, and **N**) IB analysis of markers/mediators of autophagy (LC3, p62), ER stress (CHOP, GRP-78), and mitophagy (Parkin). Ub, ubiquitylated proteins. (**J**) Mitochondrial fragmentation was assessed by immunostaining for Tom20, as detailed in Figure 7G. (**K** and **L**) Mouse acinar cells were treated for 16 hours with LDL (30 μg/mL) or the combination of LDL and 10 μM U18666A. (**M** and **N**) Mice received injections of U18666A as detailed in Figure 9B. Pancreas histopathology (H&E staining; **M**) and levels of autophagy markers/mediators (**N**) were measured. Each symbol in **A**–**F** and **I** represents an individual mouse or cell preparation. Values are mean ± SEM from 3 to 7 mice or cell preparations per condition. $^{\S}P < 0.05$, $^{\S\S}P < 0.01$ vs. control cells (without MCD/MCD-Chol). $^{***}P < 0.001$ vs. saline-treated mice. $^{\#}P < 0.05$, $^{\#\#}P < 0.01$, $^{\#\#\#}P < 0.001$ vs. CER-AP alone (no inhibitors). Significance was determined by 2-tailed Student's *t* test (**A**–**D**) or 1-way ANOVA followed by Tukey's multiple comparison test (**E**, **F**, and **I**). Scale bars: 10 μm.

We show that *Gnptab*$^{-/-}$ mice spontaneously develop pancreatitis with all key manifestations of human disease. Together with recent studies (8–11, 65), the results support our conjecture (5) that secretory cells, such as pancreatic acinar cells, rely heavily on efficient endolysosomal functions and autophagy and are particularly sensitive to their impairment. In particular, the basal secretion was significantly decreased in *Gnptab*$^{-/-}$ acinar cells. In addition, a recent study (66) showed that efficient lysosomal proteolytic degradation is required for cellular reprogramming into a regenerative phenotype and that *Gnptab* deficiency profoundly impairs the pancreas's ability to regenerate after CER-induced injury.

Prompted by the results in *Gnptab*$^{-/-}$, we found that experimental pancreatitis in WT mouse and ex vivo models greatly perturbed acinar cell cholesterol metabolism. Similar to *Gnptab*$^{-/-}$ pancreas, total cholesterol content was elevated in several unrelated acute pancreatitis models. Experimental pancreatitis caused cholesterol accumulation in LE/Ly and autolysosomes, reduced free cholesterol in the plasma membrane, and increased the expression of proteins mediating cholesterol synthesis, LDLR levels, and mitochondrial cholesterol. Both *Gnptab* ablation and experimental pancreatitis disrupted cholesterol transport through LE/Ly but by different mechanisms; the former reduced the NPC2 level, while the latter decreased NPC1 (as well as LAMP2 [ref. 8], another LE/Ly cholesterol transporter).

We showed that cholesterol is involved in the regulation of intra-acinar trypsinogen activation, a signature pancreatitis response, the mechanism of which remains obscure (6, 43, 67, 68). Trypsin activity increased with cholesterol overload, while in both *Gnptab*$^{-/-}$ acinar cells and WT experimental pancreatitis it was reduced by decreasing cholesterol content with different approaches. Inhibiting cholesterol turnover with U18666A caused impaired autophagy and ER stress in acinar cells, whereas alleviating cholesterol overload with T090137 or simvastatin reduced these and other pathologic responses of experimental pancreatitis. Simvastatin also abrogated the increase in pancreatic MLN64 caused by CER-AP. Collectively, the results reveal the critical role of cholesterol in maintaining acinar cell homeostasis and implicate its derangement in pancreatitis development.

The finding of manifestations of disordered acinar cell cholesterol homeostasis in human pancreatitis supports our conclusions from mouse and cellular models. In particular, the reduction in NPC1, together with our previous finding of a dramatic LAMP2 decrease in human pancreatitis (8), strongly indicate deranged cholesterol trafficking through LE/Ly in human disease. The decrease in pancreatic GNPTAB levels, observed in both human disease and an experimental model, further justifies *Gnptab*$^{-/-}$ mice as a genetic pancreatitis model.

Dysregulation of acinar cell cholesterol is a previously unrecognized pathology of pancreatitis. In fact, very little is known about basal cholesterol metabolism in the exocrine pancreas, the maintenance of which should be critical for acinar cells, as zymogen granule formation, secretion, and membrane recycling/retrieval all require precise and adequate lipid supply. One likely reason for this lack of knowledge is that human pancreatitis has not been associated with changes in blood cholesterol. This disconnect is reminiscent of NPC patients who have normal serum cholesterol levels despite fatal defects in cholesterol metabolism in many organs (69, 70). Likewise, we did not observe changes in serum cholesterol in either *Gnptab*$^{-/-}$ or experimental pancreatitis.

However, there have been epidemiologic studies on the effects of statins on pancreatitis severity in patients, with contradictory findings (71–74), and a clinical trial (NCT02743364) is ongoing on simvastatin's effect in alleviating pancreatitis. The premise of the above studies (as well as a recent study in a mouse pancreatitis model; ref. 75) is that statins may alter pancreatitis severity through off-target effects, particularly on inflammation; changes in pancreatic cholesterol were not investigated in patients with pancreatitis. However, the prevailing opinion is shifting toward recognizing statins' potential for pharmacologic prevention of pancreatitis (74). Cholesterol dyshomeostasis is increasingly recognized as a key player in other multifactorial diseases, such as neurodegenerative (e.g., Alzheimer's) diseases, in which it is considered a novel target for treatment (76). Our study provides evidence for categorizing pancreatitis as a cholesterol disorder disease and elucidates the mechanisms of the effects of cholesterol-lowering drugs in pancreatitis.

## Methods

Detailed description of the methods is given in the supplemental material.

*Antibodies*. Antibodies against the following proteins were purchased from Cell Signaling Technology: ATG12 (catalog 4180), Beclin1 (catalog 3495), ATG7 (catalog 2631), CHOP (catalog 5554), LC3B (catalog 2775), SQSTM1/p62 (catalog 5114), phospho-NF-κB p65/Ser536 (catalog 3033), p44/42 MAPK (ERK1/2; catalog 4696 and 9102), phospho-STAT3/Tyr705 (catalog 9145), and STAT3 (catalog 9139). Antibodies against the following proteins were purchased from Abcam: CD3 (catalog ab119332), F4/80 (catalog ab6640), LAMP1 (catalog ab24170), Rab5 (catalog ab18211), Rab9 (catalog ab2810), and SREBP2 (catalog ab30682). Antibodies against the following proteins were purchased from Santa Cruz Biotechnology: EEA1 (catalog sc-137130),

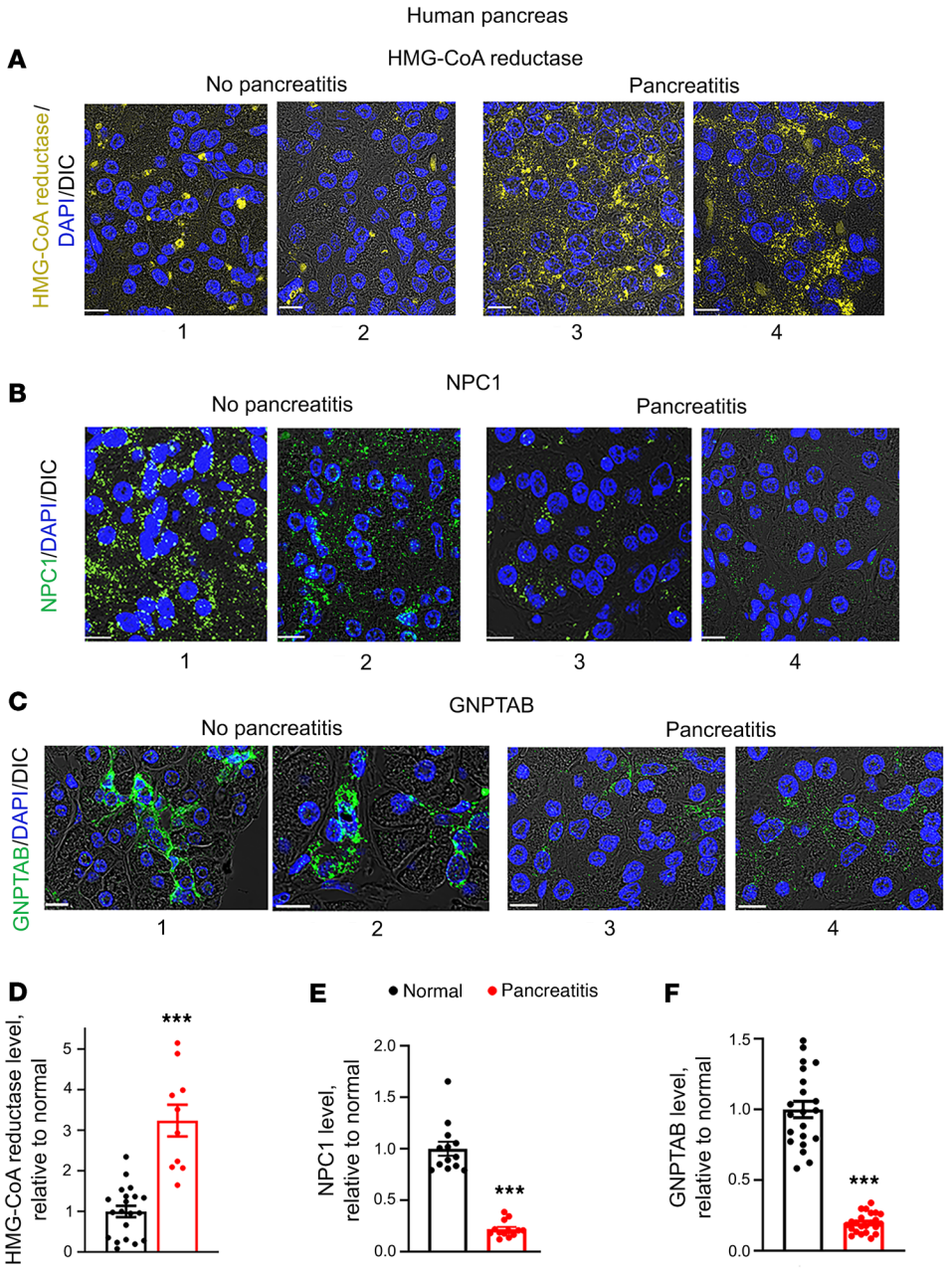


**Figure 11. Manifestations of disordered cholesterol homeostasis in human pancreatitis.** (**A**–**F**) Immunofluorescence intensity of indicated proteins in human pancreatic tissue sections was quantified with Volocity software, normalized to the number of nuclei (DAPI) in the field, and is expressed relative to that in normal pancreas. Each panel in **A**–**C** is from a different patient (from a total of 21 patients; see Supplemental Table 1). Scale bars: 10 μm. (**D**–**F**) Values are mean ± SEM; each symbol corresponds to 20 to 30 cells in a different field ($n$ = 10–23 fields from 10 without pancreatitis and 11 pancreatitis patients). ***$P < 0.001$ vs. normal human pancreas (no pancreatitis); 2-tailed Student's $t$ test.

LAMP1 (catalog sc-17768), LDLR (catalog sc-18823), NF-κB p65 (catalog sc-8008), trypsinogen (catalog sc-137077), and ubiquitin (catalog sc-8017). Antibodies against the following proteins were purchased from Sigma-Aldrich: α-amylase (catalog A8273), LAMP2 (catalog L0668), and Rab7 (catalog R8779). Antibodies against other proteins were purchased from the following companies: cadherin (Novus, catalog NB200-59), EPG5 (Byorbyt, catalog orb323262), perilipins 2 and 5 (ProGen, catalog GP40 and GP31), perilipin 3 (ProSci, catalog 3881), myeloperoxidase (Thermo Fisher Scientific, catalog PA5-16672), and MLN64/STARD3 (Invitrogen, catalog PAS-76266).

*Reagents*. CellLight Early Endosomes-GFP and Late Endosomes-RFP BacMam 2.0 were from Thermo Fisher Scientific (catalog C10586 and C10589, respectively); Cholesterol and Triglyceride Assay kits, from Abcam (catalog ab65390 and ab65336); HR series NEFA-HR2 kits to measure free fatty acids, from Wako Diagnostics (catalog 991-34891); LDL Uptake and ALT Assay kits, from Abcam (catalog ab133127 and ab105134); and AST Assay kit, from Sigma-Aldrich (catalog MAK055).

Experimental pancreatitis models in mice were performed as described previously (8, 31, 46, 48, 77) and detailed in the supplemental material. All the experiments were performed on mice of both sexes if not stated otherwise.

*Genetically modified mice*. *Gnptab*$^{-/-}$ (18, 19) and *Lamp2*$^{-/-}$ mice (8, 78) have been described. *Atg5*$^{fl/-}$ mice, obtained from Masaki Ohmuraya (Department of Genetics, Hyogo College of Medicine, Nishinomiya, Hyogo, Japan) (79), were crossed with *Pdx1-Cre* driver mice to generate *Atg5*$^{fl/-}$*;Pdx1-Cre* mice (termed *Atg5*$^{\Delta pan}$) in which the *Atg5* gene is specifically ablated in pancreatic epithelial cells. Control mice were littermates with all WT alleles. All these strains of mice are on the C57BL/6 genetic background and have been bred for at least 10 generations.

*Human pancreas specimens*. Formalin-fixed, paraffin-embedded samples of human normal pancreas and pancreatitis (see supplemental material) were deidentified and provided by the Pancreas Tissue Bank of the UCLA Department of Pathology. Tissue sections were evaluated for quality and the presence of an acinar compartment (8, 46).

Human pancreas slices (80) were obtained as detailed in the supplemental material.

Ex vivo pancreatitis models were performed on mouse and human acinar cells, and human pancreas slices by incubation with supramaximal CCK (100 nM) or carbachol (1 mM), as described previously (80, 81).

*Lipidomics*. Unbiased complex lipid analysis of pancreatic samples was performed by the NIH West Coast Metabolomics Center (UC Davis) using ultra-high-pressure liquid chromatography and tandem mass spectrometry.

*Statistics*. Statistical analysis of the results was performed with Prism 8 (GraphPad Software) using a 2-tailed Student's *t* test for comparison between 2 groups and 1-way ANOVA with Tukey's post hoc test for comparison between multiple groups. Values are expressed as mean ± SEM; a *P* value of less than 0.05 was considered significant. Statistical details for each experiment, including *n* values, are provided in figure legends.

*Study approval*. All experimental protocols were approved by the animal research committee of VA Greater Los Angeles Healthcare System in accordance with the US NIH *Guide for the Care and Use of Laboratory Animals* (National Academies Press, 2011). Deidentified formalin-fixed, paraffin-embedded samples of human normal pancreas and pancreatitis were provided by the UCLA Pancreas Tissue Bank according to a protocol approved by UCLA institutional review board. Human pancreatic slices from portions of live normal human pancreata from preterminal donors that were not used for transplantation and diverted to research (provided by Trillium Gift of Life Network, Toronto, Ontario), or from normal portions of pancreatic cancer operations, were obtained according to protocols approved by the University of Toronto institutional review board.

## Author contributions

ASG and IG designed the research. OAM, ETV, NS, CJMW, DLD, SM, YX, TT, and SWF acquired data. OAM, SWF, SJB, NOD, FSG, IG, and ASG analyzed and interpreted the data. HYG, FSG, and DWD provided tools and materials. DWD evaluated tissue sections for quality and the presence of an acinar compartment. FSG and SJP provided expertise and feedback. ASG and IG wrote the manuscript. ASG, IG, OAM, SJP, and ZR obtained funding. ASG supervised the study.

## Acknowledgments

This work was supported, at least in part, by the NIH Program Project grant P01DK098108 and the US Veterans Administration Merit Review award BX004306 (both to ASG), the NIH Southern California Research Center for ALPD and Cirrhosis P50AA11999 (to ASG, IG, and OAM), the US Department of Defense Focused Program Award W81XWH1910888 (to SJP), NIH grants DK119437 and P30DK052574 (both to NOD), and a Rosztoczy Foundation grant (to ETV). The authors are grateful to the Trillium Gift of Life Network and to the Toronto General Hospital/University Health Network Program in Biospecimen Sciences for providing human pancreatic tissue samples. We thank Vijay Singh (Mayo Clinic, Phoenix-Scottsdale, Arizona) for critical discussion of results, Bryan Roberts (West Coast Metabolomics Center, UC Davis, California) for help with lipidomics analysis, and Linsey Stiles (UCLA Mitochondria and Metabolomic Core) for help with SeaHorse measurements. It is with great sorrow that the authors acknowledge the passing, on December 28, 2020, of Samuel W. French, a world expert in pancreas and liver pathology.

Address correspondence to: Anna S. Gukovskaya or Ilya Gukovsky, Pancreatic Research Group, UCLA/West Los Angeles VA Healthcare Center, 11301 Wilshire Blvd, Blg 258, Rm 340, Los Angeles, California 90073, USA. Phone: 1.818.519.4821; Email: agukovsk@ucla.edu (ASG); Email: igukovsk@ucla.edu (IG).

ETV's present address is: Hirslanden Klinik, Bern, Switzerland.

SM's present address is: Department of Pediatric Gastroenterology, Emory University, Atlanta, Georgia, USA.

1. Pandol SJ, et al. Acute pancreatitis: bench to the bedside. *Gastroenterology*. 2007;132(3):1056–1151. Erratum: ibid, 133(3):1056.
2. Peery AF, et al. Burden and cost of gastrointestinal, liver, and pancreatic diseases in the United States: update 2018. *Gastroenterology*. 2019;156(1):254–272.
3. Lerch MM, Gorelick FS. Models of acute and chronic pancreatitis. *Gastroenterology*. 2013;144(6):1180–1193.
4. Maléth J, et al. Alcohol disrupts levels and function of the cystic fibrosis transmembrane conductance regulator to promote development of pancreatitis. *Gastroenterology*. 2015;148(2):427–439.
5. Gukovskaya AS, et al. Recent insights into the pathogenic mechanism of pancreatitis: role of acinar cell organelle disorders. *Pancreas*. 2019;48(4):459–470.
6. Mareninova OA, et al. Impaired autophagic flux mediates acinar cell vacuole formation and trypsinogen activation in rodent models of acute pancreatitis. *J Clin Invest*. 2009;119(11):3340–3355.
7. Habtezion A, et al. Acute pancreatitis: a multi-faceted set of organellar, cellular and organ interactions. *Gastroenterology*. 2019;156(7):1941–1950.
8. Mareninova OA, et al. Lysosome associated membrane proteins maintain pancreatic acinar cell homeostasis: LAMP-2 deficient mice develop pancreatitis. *Cell Mol Gastroenterol Hepatol*. 2015;1(6):678–694.
9. Diakopoulos KN, et al. Impaired autophagy induces chronic atrophic pancreatitis in mice via sex- and nutrition-dependent processes. *Gastroenterology*. 2015;148(3):626–638.
10. Antonucci L, et al. Basal autophagy maintains pancreatic acinar cell homeostasis and protein synthesis and prevents ER stress. *Proc Natl Acad Sci U S A*. 2015;112(45):E6166–E6174.
11. Wang S, et al. Impaired TFEB-mediated lysosomal biogenesis promotes the development of pancreatitis in mice and is associated with human pancreatitis. *Autophagy*. 2019;15(11):1954–1969.
12. Kornfeld S. Trafficking of lysosomal enzymes in normal and disease states. *J Clin Invest*. 1986;77(1):1–6.
13. Ghosh P, et al. Mannose 6-phosphate receptors: new twists in the tale. *Nat Rev Mol Cell Biol*. 2003;4(3):202–212.
14. Braulke T, Bonifacino JS. Sorting of lysosomal proteins. *Biochim Biophys Acta*. 2009;1793(4):605–614.
15. Koehne T, et al. Mannose 6-phosphate-dependent targeting of lysosomal enzymes is required for normal craniofacial and dental development. *Biochim Biophys Acta*. 2016;1862(9):1570–1580.
16. Coutinho MF, et al. Mannose-6-phosphate pathway: a review on its role in lysosomal function and dysfunction. *Mol Genet Metab*. 2012;105(4):542–550.
17. Tiede S, et al. Mucolipidosis II is caused by mutations in GNPTA encoding the alpha/beta GlcNAc-1-phosphotransferase. *Nat Med*. 2005;11(10):1109–1112.
18. Gelfman CM, et al. Mice lacking alpha/beta subunits of GlcNAc-1-phosphotransferase exhibit growth retardation, retinal degeneration, and

secretory cell lesions. *Invest Ophthalmol Vis Sci*. 2007;48(11):5221–5228.
19. Boonen M, et al. Vacuolization of mucolipidosis type II mouse exocrine gland cells represents accumulation of autolysosomes. *Mol Biol Cell*. 2011;22(8):1135–1147.
20. Helin H, et al. Pancreatic acinar ultrastructure in human acute pancreatitis. *Virchows Arch A Pathol Anat Histol*. 1980;387(3):259–270.
21. Aho HJ, et al. Human acute pancreatitis: a light and electron microscopic study. *Acta Pathol Microbiol Immunol Scand A*. 1982;90(5):367–373.
22. Gukovskaya AS, Gukovsky I. Autophagy and pancreatitis. *Am J Physiol Gastrointest Liver Physiol*. 2012;303(9):G993–G1003.
23. Ikonen E. Cellular cholesterol trafficking and compartmentalization. *Nat Rev Mol Cell Biol*. 2008;9(2):125–138.
24. Martin LA, et al. Mitochondrial cholesterol: mechanisms of import and effects on mitochondrial function. *J Bioenerg Biomembr*. 2016;48(2):137–151.
25. Maxfield FR, van Meer G. Cholesterol, the central lipid of mammalian cells. *Curr Opin Cell Biol*. 2010;22(4):422–429.
26. Mesmin B, et al. Insights into the mechanisms of sterol transport between organelles. *Cell Mol Life Sci*. 2013;70(18):3405–3421.
27. Rowan AD, et al. Rat procathepsin B. Proteolytic processing to the mature form in vitro. *J Biol Chem*. 1992;267(22):15993–15999.
28. Markmann S, et al. Quantitative proteome analysis of mouse liver lysosomes provides evidence for mannose 6-phosphate-independent targeting mechanisms of acid hydrolases in mucolipidosis II. *Mol Cell Proteomics*. 2017;16(3):438–450.
29. Tartakoff AM, Jamieson JD. Subcellular fractionation of the pancreas. *Methods Enzymol*. 1974;31:41–59.
30. Saluja A, et al. Subcellular redistribution of lysosomal enzymes during caerulein-induced pancreatitis. *Am J Physiol*. 1987;253(4 pt 1):G508–G516.
31. Mareninova OA, et al. Transgenic expression of GFP-LC3 perturbs autophagy in exocrine pancreas and acute pancreatitis responses in mice. *Autophagy*. 2020;16(11):2084–2097.
32. Klionsky DJ, et al. Guidelines for the use and interpretation of assays for monitoring autophagy (4th edition)[1]. *Autophagy*. 2021;17(1):1–382.
33. Zhao H, et al. Mice deficient in Epg5 exhibit selective neuronal vulnerability to degeneration. *J Cell Biol*. 2013;200(6):731–741.
34. Haas AK, et al. A GTPase-activating protein controls Rab5 function in endocytic trafficking. *Nat Cell Biol*. 2005;7(9):887–893.
35. Hsu VW, et al. Getting active: protein sorting in endocytic recycling. *Nat Rev Mol Cell Biol*. 2012;13(5):323–328.
36. Baumann JM, et al. Metabolic assays for detection of neutral fat stores. *Bio Protoc*. 2015;5(12):e1511.
37. Singh R, et al. Autophagy regulates lipid metabolism. *Nature*. 2009;458(7242):1131–1135.
38. Sztalryd C, Brasaemle DL. The perilipin family of lipid droplet proteins: Gatekeepers of intracellular lipolysis. *Biochim Biophys Acta Mol Cell Biol Lipids*. 2017;1862(10 pt B):1221–1232.
39. Garver WS, Heidenreich RA. The Niemann-Pick C proteins and trafficking of cholesterol through the late endosomal/lysosomal system. *Curr Mol Med*. 2002;2(5):485–505.
40. Willenborg M, et al. Mannose 6-phosphate receptors, Niemann-Pick C2 protein, and lysosomal cholesterol accumulation. *J Lipid Res*. 2005;46(12):2559–2569.
41. Schmidt K, et al. Regulated apical secretion of zymogens in rat pancreas. Involvement of the glycosylphosphatidylinositol-anchored glycoprotein GP-2, the lectin ZG16p, and cholesterol-glycosphingolipid-enriched microdomains. *J Biol Chem*. 2001;276(17):14315–14323.
42. Otani T, et al. Codistribution of TAP and the granule membrane protein GRAMP-92 in rat caerulein-induced pancreatitis. *Am J Physiol*. 1998;275(5):G999–G1009.
43. Saluja AK, et al. Why does pancreatic overstimulation cause pancreatitis? *Annu Rev Physiol*. 2007;69:249–269.
44. Halangk W, et al. Role of cathepsin B in intracellular trypsinogen activation and the onset of acute pancreatitis. *J Clin Invest*. 2000;106(6):773–781.
45. Mahammad S, Parmryd I. Cholesterol depletion using methyl-β-cyclodextrin. *Methods Mol Biol*. 2015;1232:91–102.
46. Biczo G, et al. Mitochondrial dysfunction, through impaired autophagy, leads to endoplasmic reticulum stress, deregulated lipid metabolism, and pancreatitis in animal models. *Gastroenterology*. 2018;154(3):689–703.
47. Mukherjee R, et al. Mechanism of mitochondrial permeability transition pore induction and damage in the pancreas: inhibition prevents acute pancreatitis by protecting production of ATP. *Gut*. 2016;65(8):1333–1346.
48. Shalbueva N, et al. Effects of oxidative alcohol metabolism on the mitochondrial permeability transition pore and necrosis in a mouse model of alcoholic pancreatitis. *Gastroenterology*. 2013;144(2):437–446.
49. Yoo SM, Jung YK. A molecular approach to mitophagy and mitochondrial dynamics. *Mol Cells*. 2018;41(1):18–26.
50. Qu Q, et al. Fatty acid oxidation and carnitine palmitoyltransferase I: emerging therapeutic targets in cancer. *Cell Death Dis*. 2016;7:e2226.
51. Aon MA, et al. Mitochondrial and cellular mechanisms for managing lipid excess. *Front Physiol*. 2014;5:282.
52. Su X, et al. Accumulation of long-chain acylcarnitine and 3-hydroxy acylcarnitine molecular species in diabetic myocardium: identification of alterations in mitochondrial fatty acid processing in diabetic myocardium by shotgun lipidomics. *Biochemistry*. 2005;44(13):5234–5245.
53. McCann MR, et al. L-carnitine and acylcarnitines: mitochondrial biomarkers for precision medicine. *Metabolites*. 2021;11(1):51.
54. Solsona-Vilarrasa E, et al. Cholesterol enrichment in liver mitochondria impairs oxidative phosphorylation and disrupts the assembly of respiratory supercomplexes. *Redox Biol*. 2019;24:101214.
55. Charman M, et al. MLN64 mediates egress of cholesterol from endosomes to mitochondria in the absence of functional Niemann-Pick Type C1 protein. *J Lipid Res*. 2010;51(5):1023–1034.
56. Balboa E, et al. MLN64 induces mitochondrial dysfunction associated with increased mitochondrial cholesterol content. *Redox Biol*. 2017;12:274–284.
57. Liscum L, Faust JR. The intracellular transport of low density lipoprotein-derived cholesterol is inhibited in Chinese hamster ovary cells cultured with 3-beta-[2-(diethylamino)ethoxy]androst-5-en-17-one. *J Biol Chem*. 1989;264(20):11796–11806.
58. Schneede A, et al. Role for LAMP-2 in endosomal cholesterol transport. *J Cell Mol Med*. 2011;15(2):280–295.
59. Hong C, Tontonoz P. Liver X receptors in lipid metabolism: opportunities for drug discovery. *Nat Rev Drug Discov*. 2014;13(6):433–444.
60. Kashiwagi K, et al. Expression of liver X receptors in normal and refractory carcinoma tissues of the human lung and pancreas. *Histol Histopathol*. 2018;33(5):497–505.
61. Hammel I, Alroy J. The effect of lysosomal storage diseases on secretory cells: an ultrastructural study of pancreas as an example. *J Submicrosc Cytol Pathol*. 1995;27(2):143–160.
62. Weintraub H, et al. Morphometric studies of pancreatic acinar granule formation in NCTR-BALB/c mice. *J Cell Sci*. 1992;102(pt 1):141–147.
63. Elleder M, Martin JJ. Mucolipidosis type II with evidence of a novel storage site. *Virchows Arch*. 1998;433(6):575–578.
64. Meister T, et al. Missorting of cathepsin B into the secretory compartment of CI-MPR/IGFII-deficient mice does not induce spontaneous trypsinogen activation but leads to enhanced trypsin activity during experimental pancreatitis — without affecting disease severity. *J Physiol Pharmacol*. 2010;61(5):565–575.
65. Li N, et al. Loss of acinar cell IKKα triggers spontaneous pancreatitis in mice. *J Clin Invest*. 2013;123(5):2231–2243.
66. Willet SG, et al. Regenerative proliferation of differentiated cells by mTORC1-dependent paligenosis. *EMBO J*. 2018;37(7):e98311.
67. De Faveri F, et al. LAP-like non-canonical autophagy and evolution of endocytic vacuoles in pancreatic acinar cells. *Autophagy*. 2020;16(7):1314–1331.
68. Sendler M, Lerch MM. The complex role of trypsin in pancreatitis. *Gastroenterology*. 2020;158(4):822–826.
69. Vanier MT, Latour P. Laboratory diagnosis of Niemann-Pick disease type C: the filipin staining test. *Methods Cell Biol*. 2015;126:357–375.
70. Cluzeau CV, et al. Microarray expression analysis and identification of serum biomarkers for Niemann-Pick disease, type C1. *Hum Mol Genet*. 2012;21(16):3632–3646.
71. Kuoppala J, et al. Use of statins and the risk of acute pancreatitis: a population-based case-control study. *Pharmacoepidemiol Drug Saf*. 2015;24(10):1085–1092.
72. Lin CM, et al. Use of simvastatin and risk of acute pancreatitis: a nationwide case-control study in Taiwan. *J Clin Pharmacol*. 2017;57(7):918–923.
73. Wu BU, et al. Simvastatin is associated with reduced risk of acute pancreatitis: findings from a regional integrated healthcare system. *Gut*. 2015;64(1):133–138.
74. Machicado JD, Papachristou GI. Pharmacologic

management and prevention of acute pancreatitis. *Curr Opin Gastroenterol*. 2019;35(5):460–467.
75. Piplani H, et al. Simvastatin induces autophagic flux to restore cerulein-impaired phagosome-lysosome fusion in acute pancreatitis. *Biochim Biophys Acta Mol Basis Dis*. 2019;1865(11):165530.
76. Loera-Valencia R, et al. Alterations in cholesterol metabolism as a risk factor for developing Alzheimer's disease: Potential novel targets for treatment. *J Steroid Biochem Mol Biol*. 2019;190:104–114.
77. Mareninova OA, et al. Cell death in pancreatitis: caspases protect from necrotizing pancreatitis. *J Biol Chem*. 2006;281(6):3370–3381.
78. Tanaka Y, et al. Accumulation of autophagic vacuoles and cardiomyopathy in LAMP-2-deficient mice. *Nature*. 2000;406(6798):902–906.
79. Hashimoto D, et al. Involvement of autophagy in trypsinogen activation within the pancreatic acinar cells. *J Cell Biol*. 2008;181(7):1065–1072.
80. Liang T, et al. Ex vivo human pancreatic slice preparations offer a valuable model for studying pancreatic exocrine biology. *J Biol Chem*. 2017;292(14):5957–5969.
81. Lugea A, et al. Human pancreatic acinar cells: proteomic characterization, physiologic responses, and organellar disorders in ex vivo pancreatitis. *Am J Pathol*. 2017;187(12):2726–2743.